Earth Planet. Sci. Lett. 696 (2026) 120354



Contents lists available at ScienceDirect

Earth and Planetary Science Letters

journal homepage: www.elsevier.com/locate/epsl



Sensitivity of neutrino oscillations to the Earth's interior properties

Isabel A. Goos [a,b,*], Nobuaki Fuji [b,c], Stéphanie Durand [d], Véronique Van Elewyck [a,c], João A. B. Coelho [a], Eric Mittelstaedt [e], Yael Deniz [e]

[a] Université Paris Cité, CNRS, Astroparticule et Cosmologie, Paris, F-75013, France
[b] Université Paris Cité, Institut de physique du globe de Paris, CNRS, Paris, F-75005, France
[c] Institut universitaire de France, Paris, France
[d] Université Claude Bernard Lyon 1, ENS de Lyon, CNRS, UMR 5276 LGL-TPE, Villeurbanne, France
[e] University of Idaho, Department of Earth and Spatial Sciences, Moscow, 83844, Idaho, USA

ARTICLE INFO

Editor: Dr C Carolina Lithgow-Bertelloni

Keywords:
Earth's interior
Atmospheric neutrinos
Neutrino oscillations
Density profile inversion
Seismology

ABSTRACT

Understanding the Earth's deep interior remains challenging, as traditional geophysical methods face ambiguities in linking seismic observations to temperature, composition, or mass density variations. Atmospheric neutrinos, produced by the constant flux of cosmic rays colliding with the upper atmosphere, offer a complementary probe: with energies of a few GeV, they traverse the Earth and experience flavor oscillations influenced by the planet's electron density distribution, which depends on both its mass density and composition. Combining seismic observations with neutrino measurements in a joint inversion framework could provide complementary constraints on gross spatial and compositional variations in the deep Earth. We consider the next-generation neutrino detectors KM3NeT/ORCA, Hyper-Kamiokande, and DUNE, as well as an idealized hypothetical detector representing the intrinsic sensitivity of the method. The idealized detector is most sensitive to perturbations in the core, whereas realistic detector performance shifts the sensitivity toward the mantle, including the mantle transition zone, where hydrogen enrichment could produce detectable variations in electron density. These results establish the sensitivity of neutrino oscillations to the Earth's electron density profile and provide a basis for future joint neutrino–seismic tomography.

1. Introduction

Direct exploration of the Earth's interior is limited to depths of approximately 12 km, corresponding to the deepest borehole ever drilled (Kozlovsky and Adrianov, 1987). Consequently, understanding the planet's interior has relied on indirect methods. Among these, seismology (Aki et al., 1976; Sengupta and Toksöz, 1976; Fichtner et al., 2024) has been particularly successful in revealing its internal 3D structure through inversion of seismic data. Seismologists use either full seismic waveforms (Fichtner, 2010) or their secondary attributes such as the travel times of body waves (Aki et al., 1976; Sengupta and Toksöz, 1976; Hosseini et al., 2020) and the dispersion of surface waves (Montagner and Tanimoto, 1990; Durand et al., 1999; Debayle et al., 2016), or a combination of these (Durand et al., 2016, 2017; Ritsema et al., 2011; Koelemeijer et al., 2015). Both approaches constrain seismological parameters, such as isotropic and anisotropic seismic velocities, and attenuation, which are then used to infer physical properties of the Earth's interior, such as temperature, pressure, and chemical composition. Because the sensitivity of body waves and surface waves to density is much lower than to seismic velocities, imaging density variations inside Earth has proven difficult. Free oscillations excited by large earthquakes (Mw $\geq$ 7.0) provide one of the few geophysical tools for decoupling elastic moduli and density with sufficiently strong sensitivity. This approach has helped constrain the radial density profile (Dziewonski and Anderson, 1981; Irving et al., 2018), but inferring a full 3D density structure remains challenging (Ishii and Tromp, 1999; Kuo and Romanowicz, 2002; Romanowicz, 2001).

Given the expansion of seismic networks, increased computational resources, and improvements in direct and inverse problem theory, the resolution of global 3D tomographic models has improved continuously. However, while seismic tomography effectively images structure in terms of seismic properties, inverting for temperature and composition from seismic data alone is an ill-posed problem that requires extensive assumptions and extrapolations of mineral physics, petrological, and thermochemical data (Deng et al., 2023). To address these limitations, combining multiple complementary observables, each sensitive to different physical properties, offers an alternative way to better constrain the origin of seismic heterogeneities.

* Corresponding author.
E-mail address: goos@apc.in2p3.fr (I.A. Goos).

https://doi.org/10.1016/j.epsl.2026.120354
Received 1 December 2025; Received in revised form 7 September 2026; Accepted 14 September 2026
Available online 30 September 2026
0012-821X/© 2026 The Authors. Published by Elsevier B.V. This is an open access article under the CC BY license (http://creativecommons.org/licenses/by/4.0/).

In this context, neutrino oscillation tomography of the Earth (NOTE) has recently emerged as a promising complementary approach (for a summary of early studies, see Winter (2006)). NOTE offers the possibility to probe the Earth's interior using neutrinos, naturally abundant fundamental particles that traverse the planet (Athar et al., 2022). NOTE makes use of atmospheric neutrinos, which are copiously produced in extensive air showers generated by the interaction of cosmic rays with air molecules (Chapter 24 of Tanabashi et al., 2018). Neutrinos come in three types, known as flavors: electron neutrino ν_e, muon neutrino ν_μ, and tau neutrino ν_τ, together with their antiparticles $\bar{\nu}_e$, $\bar{\nu}_\mu$, and $\bar{\nu}_\tau$. Once produced in the atmosphere, they propagate in straight lines through the Earth. As they propagate, neutrinos have a probability to change from one flavor to another, a quantum-mechanical phenomenon known as flavor oscillations. Consequently, a neutrino produced in a given flavor could be detected after some distance in a different flavor. The presence of electrons (i.e., matter) in the Earth affects these oscillation probabilities for neutrinos with energies from a few GeV to several tens of GeV. NOTE exploits this phenomenon to probe the Earth's electron-density profile, which combines matter density and chemical composition, by analyzing distortions in oscillation patterns (Rott et al., 2015; Winter, 2016; Bourret et al., 2017; Denton and Pestes, 2021; D'Olivo Saez et al., 2022; Upadhyay et al., 2023; Maderer et al., 2023b; Capozzi and Petcov, 2022; Petcov, 2024).

NOTE has not yet been performed using experimental data. The neutrino detectors Hyper-Kamiokande (HK, Abe et al. (2018)) and DUNE (Abi et al., 2020) are under construction, while KM3NeT/ORCA (Adrian-Martinez et al., 2016) has accumulated only a limited amount of data so far. Consequently, current results are limited to sensitivity projections. For DUNE, 10 years of measurements are expected to yield sensitivities of $\sim 10\%$ for the matter density of the core and lower mantle, and $\sim 20\%$ for the upper mantle (Kelly et al., 2022). HK is expected to constrain the average core density at the $\mathcal{O}(10\text{–}40\%)$ level after ~ 20 years, depending on the achieved measurement performance (Jesús-Valls et al., 2025). Similar sensitivities for the outer core ($\sim$ 15–40%) and mantle ($\sim$ 6–20%) could be achieved with 10 years of ORCA measurements (Capozzi and Petcov, 2022). While not competitive with geophysical constraints, NOTE can provide direct sensitivity to chemical composition. For instance, Maderer et al. (2023b) show that combining KM3NeT/ORCA, HK, and DUNE could discriminate FeNi from FeNiH outer-core compositions at 1σ after ~ 50 years of concomitant measurements. Neutrino measurements, while individually less constraining, could help break degeneracies inherent to geophysical probes. Finally, simulations based on the neutrino detector IceCube DeepCore, representing ~ 10 years of operation, demonstrate the ability to perform correlated density measurements of different Earth layers when incorporating constraints from the Earth's total mass and moment of inertia (Chattopadhyay et al., 2025).

In this study, we propose to exploit neutrino observables to constrain Earth's interior properties and aim to lay the groundwork for an inverse problem based on neutrino data. Solving any inverse problem requires defining the forward problem, in which the synthetic data $\mathbf{u}$, the model parameters $\mathbf{m}$, and the forward function $\mathcal{G}$ are characterized such that $\mathbf{u} = \mathcal{G}(\mathbf{m})$. In many cases progress toward inversion relies on a linearized description of this function through the Fréchet derivatives $\nabla_{\mathbf{m}}\mathcal{G}(\mathbf{m})$. In this work, we establish the mathematical framework required for neutrino oscillation based inversion and derive the associated Fréchet derivatives. We then perform a comprehensive sensitivity study of NOTE with respect to variations in Earth's physical properties. These results provide the necessary basis for a future joint inversion with seismic data.

The paper is organized as follows. After the introduction in Section 1, Section 2 contrasts neutrino and seismic observables. Section 3 introduces the forward problem $\mathcal{G}$ for NOTE. Section 4 presents the methods used in this work. The computation of Fréchet derivatives is demonstrated in Section 5, together with the presentation of the sensitivity study. We conclude with closing remarks in Section 6.

2. Neutrino oscillation tomography in comparison with seismology

This paper aims to lay the groundwork for the future joint analysis of seismic and neutrino data. Before proceeding, it is important to describe neutrino oscillation tomography of the Earth (NOTE) in comparison with seismology, as illustrated in Fig. 1. In both approaches, a probe (neutrino or wave) propagates through the Earth and is influenced by the Earth's material properties along its ray. Neutrinos are affected by the presence of electrons, whereas seismic waves are influenced by the elastic and anelastic properties of the Earth's materials. Upon detection after traversing the Earth, their observed properties reflect the characteristics of the material encountered along their ray. Hence, seismology and NOTE share a common foundation, which motivates our preparatory work toward a joint inversion. A closer look reveals important differences alongside these similarities, as discussed below.

First, the data-acquisition configurations of NOTE and terrestrial global seismology are fundamentally inverted (see Fig. 1a and b). Because of their cost, only a limited number of neutrino detectors will be deployed worldwide. Atmospheric neutrinos are produced continuously and abundantly in the Earth's atmosphere, allowing each detector to record neutrinos arriving from all directions. In contrast, earthquakes occur sporadically, whereas seismic stations are distributed globally—albeit unevenly. Additionally, seismology benefits from over five decades of accumulated observations, giving it far greater statistical power than current atmospheric neutrino data. However, next-generation neutrino detectors are expected to substantially increase the NOTE dataset in the coming decades.

Another distinction lies in the traceability of individual signals. In seismology, specific seismic phases recorded on a seismogram can be associated with well-defined propagation rays back to a specific source (Fig. 1a). By contrast, the continuous and intense nature of the atmospheric neutrino flux means that an individual neutrino cannot be traced back to the shower that produced it (Fig. 1b). Rather, for NOTE, the flux as a whole must be accurately modeled.

Another difference concerns seismic wave propagation. Seismic waves undergo reflection and refraction within the Earth's interior, leading to complex ray trajectories (Fig. 1a). Neutrinos propagate along straight rays (Fig. 1b). Consequently, once the incidence angle of a neutrino is measured, its ray, and thus the region of the Earth it probes, is uniquely constrained within uncertainties.

NOTE is based on the principle that the presence of electrons along the neutrino ray impacts its oscillation probabilities. The probability of a given oscillation process $\nu_\alpha \to \nu_\beta$ (where $\alpha, \beta \in \{e, \mu, \tau\}$) is usually visualized in a 2D plot, called oscillogram. The oscillogram is a function of neutrino energy E_ν and incidence angle θ_z, where θ_z is measured with respect to the vertical at the neutrino's exit point on the Earth's surface (Fig. 1b). Fig. 1d displays the oscillogram corresponding to the probability $P_{\nu_\mu \to \nu_\tau}$ that a muon neutrino produced in the atmosphere interacts as a tau neutrino after having propagated across the Earth. Oscillograms illustrate how oscillations transform the flavor composition of the neutrino flux traversing the Earth, capturing solely the influence of Earth's matter on oscillation probabilities, independent of the neutrino source, and subsequent detection process. They can be compared against time-distance plots in seismology (Fig. 1c). Here, seismograms are ordered as a function of distance from the source and, instead of showing the amplitudes of the seismograms, we display their envelopes, which represent the energy.

In Fig. 1d, a sudden change in the oscillation pattern occurs at an epicentral distance of $\Delta \simeq 114°$, or equivalently $\cos\theta_z \simeq -0.84$. This is due to the large jump in electron density experienced by neutrinos that sample the core compared to those that do not. The envelopes of the seismograms in Fig. 1c also exhibit a change at around 110°, where the first arrival fades. This feature, though less striking than for neutrinos, is likewise attributable to the presence of the core.

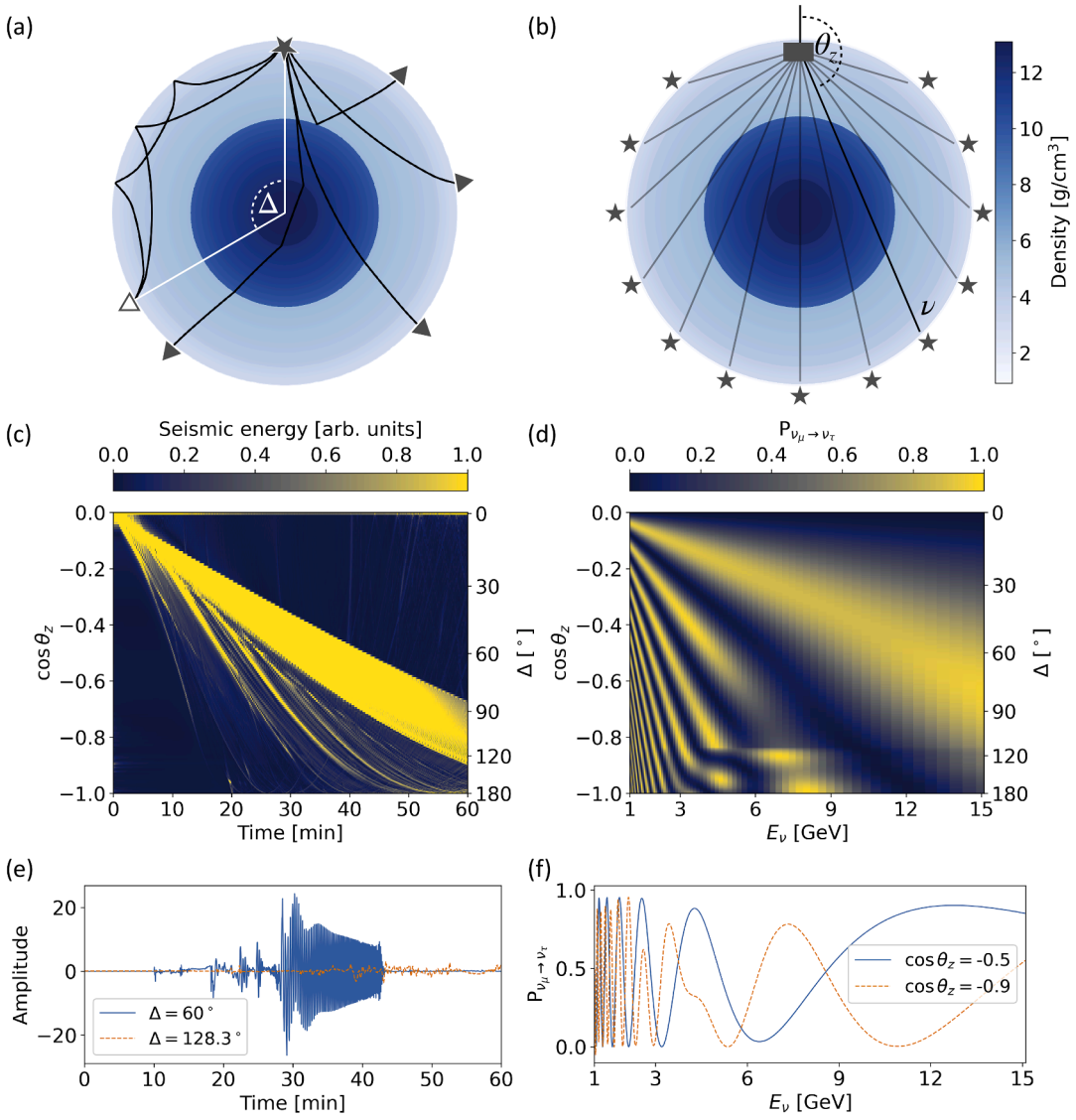


Fig. 1. Overview of the data-acquisition configurations (a and b) and recorded observations (c–f) in both global seismology (left column) and NOTE (right column). (a) Triangles represent seismic stations and the star an earthquake, with rays illustrating seismic wave paths sampling different regions of the Earth. (b) The gray rectangle denotes a neutrino detector and the stars neutrino sources, where the incidence angle θ_z is measured from the vertical at the detector and straight lines show possible neutrino rays. (c) Time–distance plot obtained by ordering the vertical components of synthetic seismograms by epicentral distance. The synthetic seismograms are calculated using the PREM model (Dziewonski and Anderson, 1981) for an earthquake at 30 km depth. We plot the envelopes of the seismograms, representing the energy arriving over time. The time is given with respect to the time of the earthquake. (d) Neutrino oscillogram representing the probability $P_{\nu_\mu \to \nu_\tau}$ as a function of neutrino energy E_ν and incidence angle θ_z. The Earth model described in Section 3.2 is used. (e) Seismic waveforms as a function of time for two particular epicentral distances Δ, 60° (blue curve) and 128.3° (dashed orange curve). (f) Oscillation probabilities as a function of energy for two particular incidence angles θ_z, equivalent to $\Delta = 60°$ (blue curve) and $\Delta = 128.3°$ (dashed orange curve), as in panel (e).

Traveltime tomography extracts first breaks or major phase onsets from seismic waveforms for numerous source–receiver pairs. Setting aside the treatment of Fresnel zones (ray theory versus finite-frequency tomography), each travel time is a scalar quantity that encodes the integral of the structure sampled along the corresponding ray. While a single travel time cannot uniquely constrain the seismic wave velocity in every voxel, the ensemble of intersecting rays enables imaging of Earth's interior. Full waveform inversion goes even further by exploiting complete time-dependent signals (Deschamps et al., 2019; French and Romanowicz, 2015; Fuji et al., 2010; Konishi et al., 2020; Virieux and Operto, 2009), which carry information from time-dependent Fresnel zones, thereby providing substantially more information about the propagation medium. Example waveforms are shown in Fig. 1e for $\Delta = 60°$ and 80°, corresponding to $\cos\theta_z = -0.5$ and -0.9, respectively.

In NOTE, when considering a single detector, neutrino rays never intersect because they travel in straight lines and their Fresnel zone is restricted to the ray itself (Fig. 1b). An analogy can be drawn with one-station seismology, such as the InSight SEIS experiment on Mars (Lognonné et al., 2020; Jacob et al., 2022). By exploiting full waveforms whose sensitivity to structure evolves over time it became possible to image the planet's interior even without crossing rays. Oscillation probabilities exhibit a characteristic dependence on energy (Fig. 1f). More importantly, the impact of perturbations in the matter properties on this probability is also energy dependent. Hence, in principle, imaging a thin column of matter using neutrinos of varying energies that traverse it is feasible, and the prospect of imaging the entire Earth using neutrinos that sample different regions motivates the present work.

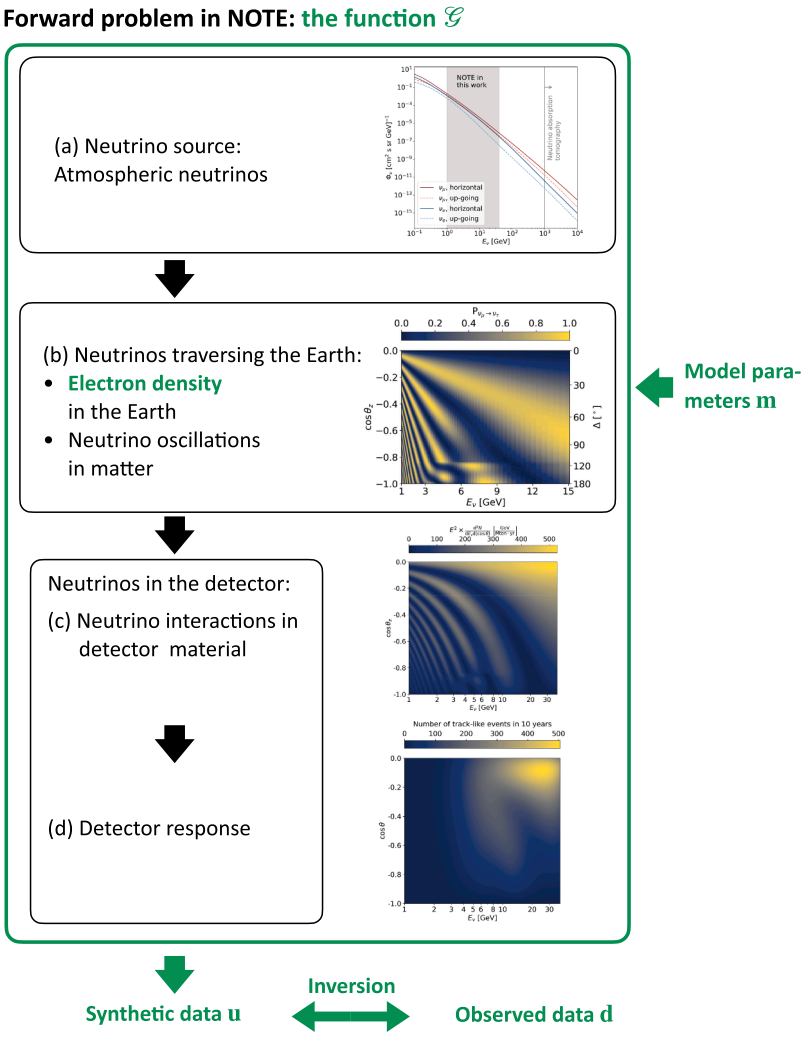


Fig. 2. Flowchart of the forward modeling of neutrino observables through the function $\mathcal{G}$. The process starts with the atmospheric neutrino flux (step (a)), as described in Section 3.1, using the model from Honda et al. (2015), with the corresponding Fig. 3 included here in miniature for illustration. Atmospheric neutrinos then traverse the Earth, parameterized by the model parameters **m**, and undergo flavor transitions (step (b)), whose probabilities depend on the electron density along their ray (Dziewonski and Anderson, 1981; McDonough, 2010; Wedepohl, 1995; Quinby-Hunt and Turehian, 1983) as well as on neutrino oscillation physics in matter (Giunti and Kim, 2007), as outlined in Section 3.2. The example oscillogram from Fig. 1d is also embedded. The figures shown within the boxes in steps (a) and (b) correspond directly to these processes (the oscillogram represents oscillation probabilities only and is independent of the neutrino flux). In the vicinity of the detector, neutrinos may interact (step (c)) and produce detectable signals (step (d)), as described in Section 3.3 (Formaggio and Zeller, 2012; Adrian-Martinez et al., 2016; Abe et al., 2018; Abi et al., 2020). Fig. 5a and b correspond to the result of coupling steps (a)–(c) and (a)–(d), respectively, and are shown outside the boxes to highlight this distinction from the figures in (a) and (b). The outcome of combining steps (a)–(d) is the synthetic data **u**, which can be compared with real measurements **d** to perform an inversion.

3. Forward modeling of neutrino observables

In this section, we outline the forward problem of NOTE, represented by the function $\mathcal{G}$, which maps Earth properties **m** to expected neutrino rates, denoted **u**. These synthetic data can be compared with observed data **d** to perform an inversion. Fig. 2 summarizes the three main components of $\mathcal{G}$: the flux of atmospheric neutrinos entering the Earth (Section 3.1), the computation of oscillation probabilities as they traverse the Earth's interior (Section 3.2), and the modeling of their detection (Section 3.3). For reference, Appendix A provides tables listing the physical constants (Tables A.1, A.3), variables (Table A.2), and expressions (Tables A.4–A.5) used in this study.

3.1. Atmospheric neutrino flux

Atmospheric neutrinos are produced in the atmosphere when cosmic rays interact with air molecules (step (a) in Fig. 2). The cosmic ray spectrum comprises nuclei ranging from hydrogen to iron, spanning energies from a few hundred MeV to $\sim 10^{14}$ MeV. The average altitude at which cosmic rays first interact with the atmosphere is nucleus-dependent. Hydrogen interacts on average at around 16 km (Blanco et al., 2009), while heavier nuclei interact at progressively higher altitudes. Other sources of shower-to-shower fluctuations, as well as atmospheric density variations, further influence neutrino production.

In this study, we use the atmospheric neutrino flux model by Honda et al. (2015). It simulates the cosmic ray flux and its interactions with the atmosphere, as well as the propagation, interactions, and decays of secondary particles, while accounting for all the sources of variability mentioned above. It provides neutrino fluxes as a function of energy and arrival direction at several reference experimental sites. The specific configuration used in this study is detailed in Appendix B.1.

The atmospheric neutrino flux decreases steeply with energy, as shown in Fig. 3 (the ν_τ and $\bar{\nu}_\tau$ contributions are negligible and thus not shown). This decline emphasizes the importance of low-energy neutri-

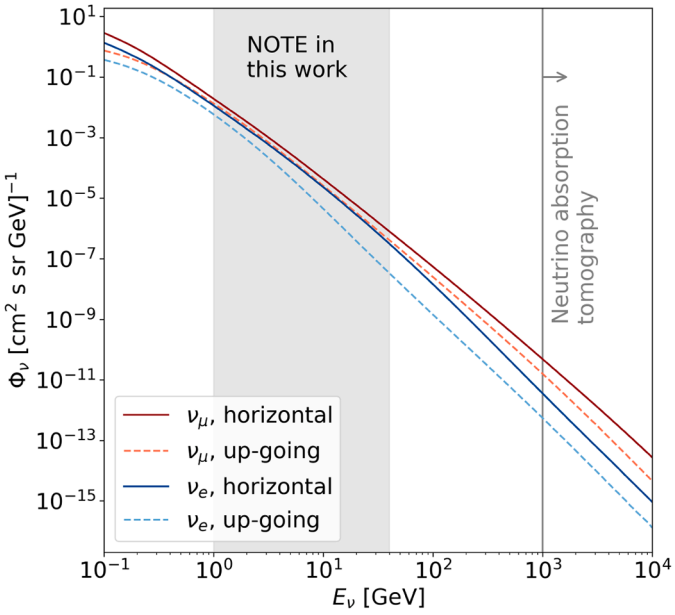


Fig. 3. Flux of atmospheric electron neutrinos (blue curves) and muon neutrinos (red curves) from Honda et al. (2015), averaged over azimuthal angle. Horizontal neutrinos (solid lines) correspond to $\cos\theta_z$ values between −0.1 and 0.0, while up-going neutrinos (dashed lines) span the range from −1.0 to −0.9. The shaded region represents the neutrino energy range considered in this work for NOTE. The vertical gray line indicates the approximate energy above which neutrino absorption becomes relevant.

nos for tomography, as they provide the larger event statistics. Neutrino absorption tomography becomes relevant above $\sim 10^3$ GeV (marked by a vertical line), where the atmospheric neutrino flux is notably lower than at energies relevant for NOTE (represented by the shaded band). The flux of neutrinos produced in astrophysical point sources is even lower and only comparable with the atmospheric neutrino flux near 10^4 GeV (Abbasi et al., 2026). Yet, the impact of Earth model perturbations on neutrino rates is larger for absorption than for oscillations, making both methods relevant for Earth tomography. While we envision a joint inversion including both approaches, in this study we focus on NOTE.

3.2. Neutrinos traversing the Earth

In this section, we outline the key aspects of flavor transitions in matter (step (b) in Fig. 2). When a neutrino is produced, its quantum state collapses to a flavor eigenstate denoted $|\nu_\alpha\rangle$, where $\alpha \in \{e, \mu, \tau\}$. Neutrino oscillations arise because eigenstates of propagation are not aligned with these flavor eigenstates.

In vacuum, the propagation eigenstates are the mass eigenstates $|\nu_j\rangle$ (with $j \in \{1, 2, 3\}$), which correspond to the possible outcomes of a neutrino mass measurement, each with a definite mass m_j. Thus, a neutrino produced in the flavor eigenstate $|\nu_\alpha\rangle$ is a superposition of the mass eigenstates:

$$|\nu_\alpha\rangle = \sum_{j=1}^{3} U_{\alpha j}^{*} \, |\nu_j\rangle \, . \tag{1}$$

U denotes the complex unitary Pontecorvo–Maki–Nakagawa–Sakata (PMNS) matrix, which performs the change of basis between the orthonormal sets of flavor and mass eigenstates:

$$U = \begin{pmatrix} 1 & 0 & 0 \\ 0 & c_{23} & s_{23} \\ 0 & -s_{23} & c_{23} \end{pmatrix} \begin{pmatrix} c_{13} & 0 & s_{13} e^{-i\delta_{\mathrm{CP}}} \\ 0 & 1 & 0 \\ -s_{13} e^{i\delta_{\mathrm{CP}}} & 0 & c_{13} \end{pmatrix} \begin{pmatrix} c_{12} & s_{12} & 0 \\ -s_{12} & c_{12} & 0 \\ 0 & 0 & 1 \end{pmatrix}. \tag{2}$$

Unitarity reduces its 18 real parameters to $s_{ij} = \sin\Theta_{ij}$, $c_{ij} = \cos\Theta_{ij}$, and δ_{CP}, after unphysical phases are absorbed into the field definitions.

If this neutrino propagates over a distance L, each $|\nu_j\rangle$ evolves with a phase Ψ that depends on its mass m_j, E_ν and L, which we leave in symbolic form for simplicity:

$$|\nu_\alpha(L)\rangle = \sum_{j=1}^{3} U_{\alpha j}^{*} \left(e^{i\Psi(m_j, E_\nu, L)} \, |\nu_j\rangle \right). \tag{3}$$

Since these phases differ for each j, the superposition at distance L is no longer the same as at production. Expressing $|\nu_\alpha(L)\rangle$ back in terms of the flavor eigenstates $|\nu_\beta\rangle$ gives

$$|\nu_\alpha(L)\rangle = \sum_{\beta=e,\mu,\tau} \left(\sum_{j=1}^{3} U_{\alpha j}^{*} e^{i\Psi(m_j, E_\nu, L)} U_{\beta j} \right) |\nu_\beta\rangle \, . \tag{4}$$

When the neutrino is detected, its quantum state collapses to a flavor eigenstate $|\nu_\beta\rangle$ ($\beta \in \{e, \mu, \tau\}$) with probability equal to the squared modulus of the corresponding coefficient:

$$\mathrm{P}_{\nu_\alpha \to \nu_\beta}(L) = \left| \sum_{j=1}^{3} U_{\alpha j}^{*} e^{i\Psi(m_j, E_\nu, L)} U_{\beta j} \right|^2 . \tag{5}$$

The complex exponentials that arise lead to sinusoidal terms in the transition probabilities, giving neutrino oscillations their name.

The expression for Ψ in Eq. (3) is obtained by solving the Schrödinger equation (which describes the temporal evolution of the neutrino, or equivalently, its evolution with distance L)

$$i\hbar \partial_t \, |\nu(t)\rangle = \mathcal{H}(t) \, |\nu(t)\rangle \, , \tag{6}$$

for each $|\nu_j\rangle$. $\mathcal{H}(t)$ is the Hamiltonian governing the system's evolution and $\hbar$ is the reduced Planck constant (i in this context refers to the complex number). In vacuum, the Hamiltonian is given by

$$\mathcal{H}_{\mathrm{vacuum}} = \frac{1}{2E_\nu} U \begin{pmatrix} 0 & 0 & 0 \\ 0 & \Delta m_{21}^2 & 0 \\ 0 & 0 & \Delta m_{31}^2 \end{pmatrix} U^{\dagger}, \tag{7}$$

where $\Delta m_{ij}^2 = m_i^2 - m_j^2$ and the $\dagger$ denotes the Hermitian conjugate. If, however, the neutrino travels through matter, the effective matter Hamiltonian

$$\mathcal{H}_{\mathrm{matter}}(t) = \begin{pmatrix} V_e(t) & 0 & 0 \\ 0 & 0 & 0 \\ 0 & 0 & 0 \end{pmatrix} \tag{8}$$

needs to be added:

$$\mathcal{H}(t) = \mathcal{H}_{\mathrm{vacuum}} + \mathcal{H}_{\mathrm{matter}}(t). \tag{9}$$

Since $\mathcal{H}_{\mathrm{vacuum}}$ is constant, the vacuum scenario (Eq. (6)) admits simple analytical solutions, which can be found in standard neutrino textbooks (see e.g. Giunti and Kim, 2007). The matter scenario, which applies to NOTE, requires a numerical solution to track neutrinos as they traverse regions of varying Earth properties (comprised in Eq. (8)). Appendix B.2 outlines the treatment of this case adopted in this work and specifies the parameters entering $\mathcal{H}_{\mathrm{vacuum}}$.

In NOTE, $\mathcal{H}_{\mathrm{matter}}$ depends on the neutrino ray through the Earth by means of the matter-induced potential

$$V_e(t) = \pm\sqrt{2} \, G_{\mathrm{F}} \, n_e(t), \tag{10}$$

where $n_e(t)$ is the electron density profile along the ray, G_{F} is the Fermi constant, and the sign is positive (negative) for neutrinos (antineutrinos). Neutrino oscillation probabilities thus depend on the electron density along the neutrino ray:

$$n_e = \frac{\rho \, Y_e \, \mathcal{N}_{\mathrm{A}}}{M_{\mathrm{u}}}, \tag{11}$$

where ρ is the matter density, Y_e is the electron yield (a dimensionless quantity representing the number of electrons per nucleon), $\mathcal{N}_{\mathrm{A}}$ is the Avogadro number, and $M_{\mathrm{u}} = 10^{-3}$ kg/mol is the molar mass constant. The electron density defined in this way is the number of electrons per unit volume.

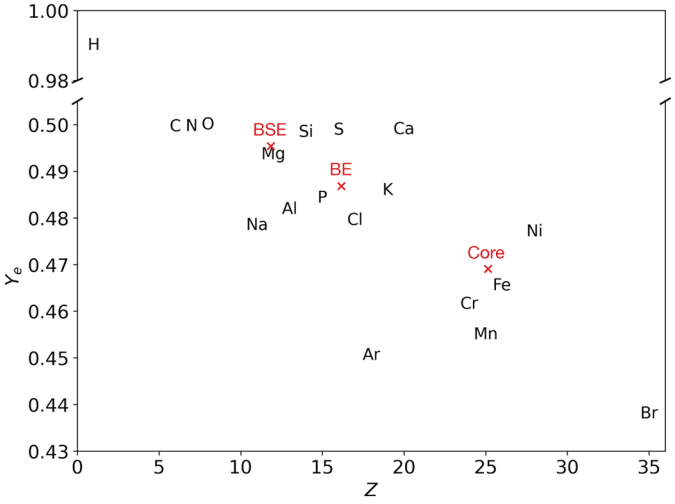


Fig. 4. Electron yield Y_e as a function of average atomic number Z for the chemical elements considered in Eq. (12) and for selected Earth materials. Chemical elements are indicated by their symbols (in black), while the red crosses denote the bulk Earth (BE), bulk silicate Earth (BSE), and the core. Note that, for pure chemical elements, the electron yield coincides with the ratio of atomic number Z to standard atomic weight A. The average atomic number of the chemical elements is obtained by considering all possible isotopes (Tuli et al., 1995), while that of the composites is calculated using the element fractions from McDonough (2010).

For our nominal (or reference) Earth model, we adopt the density profile from PREM (Dziewonski and Anderson, 1981) and compute the electron yield at each position $\bar{x}$ as:

$$Y_e(\bar{x}) = \sum_i w_i(\bar{x}) \left(\frac{Z}{A}\right)_i , \tag{12}$$

where the sum is taken over all the elements present at $\bar{x}$. The time dependence in Eq. (10) is recovered using that neutrinos travel almost at the speed of light $c = |\bar{x} - \bar{x}_{\text{entry}}|/t$, where $\bar{x}_{\text{entry}}$ is the position where the neutrino enters the Earth. w_i is the weight fraction of element i, with Z and A its atomic number and standard atomic weight, respectively. The composition is taken from McDonough (2010) if $\bar{x}$ is in the mantle or core, from Wedepohl (1995) for crustal materials, and from Quinby-Hunt and Turehian (1983) for oceanic materials (Table A.3 provides a summary of the resulting values of Y_e).

Y_e reflects chemical composition, with values ~ 0.47 in the core and ~ 0.50 in the mantle and crust. Fig. 4 shows the Y_e values for the chemical elements considered in this work (abundances above 0.01%) and for selected Earth materials (McDonough, 2010). An overall decreasing trend with Z is observed, with hydrogen standing out due to its value close to unity. This sensitivity of neutrino oscillations to composition through the electron yield further motivates the use of neutrinos to probe the Earth's interior. Eq. (11) implies that NOTE is sensitive to the combined effect of matter density ρ and composition through Y_e, which together define the model parameters $\mathbf{m}$. If ρ were independently and sufficiently well constrained, the electron density n_e could be directly related to Y_e. However, the level of precision required on ρ for this interpretation to be valid remains to be quantified.

3.3. Neutrino detection

Once neutrinos reach the vicinity of the detector, they have a small probability of interacting (step (c) in Fig. 2) and generating a detectable signature (step (d) in Fig. 2).

In the energy range of interest for NOTE, neutrinos interact primarily by scattering off nuclei in the medium (Formaggio and Zeller, 2012) (step (c) in Fig. 2). These interactions are classified as neutral-current (NC) or charged-current (CC), depending on whether a Z^0 or $W^\pm$ weak-force boson is exchanged. In NC interactions, the neutrino (antineutrino) remains in the final state and escapes the instrumented detector volume, while the scattered nucleus can produce a detectable signal. NC interactions are flavor-independent (and thus not sensitive to oscillations), giving two possible interaction channels, denoted as ν NC and $\bar{\nu}$ NC. In CC interactions, the incoming neutrino (antineutrino) ν_α ($\bar{\nu}_\alpha$), with $\alpha \in \{e, \mu, \tau\}$, produces a negatively (positively) charged particle α^- (α^+). Both the scattered nucleus and the outgoing charged particle can produce detectable signals, resulting in six possible interaction channels: ν_α CC and $\bar{\nu}_\alpha$ CC, for $\alpha \in \{e, \mu, \tau\}$. The probability for any of these eight interaction channels to occur depends on the detection medium and scales linearly with the number of nuclear targets, i.e., the detector mass.

Combining steps (a)–(c) in Fig. 2 yields the expected number of interacting events in a given detector (see Appendix B.3 for the implementation in this work). Fig. 5a shows the expected distribution of $(\nu_\mu + \bar{\nu}_\mu)$ CC events for an exposure of 1 Mton-year, defined as the product of detector mass and data-acquisition period. This quantity characterizes the event statistics and depends only on the detector material through the interaction probabilities of the different channels (a water detection medium is assumed in Fig. 5a). Comparing these distributions for different Earth models $\mathbf{m}$ helps identify those interaction channels and regions in $(E_\nu, \cos\theta_z)$ space that carry the strongest inherent discriminating signal.

In practice, observations $\mathbf{d}$ are affected by the limited efficiency and detection resolution of real detectors, where efficiency refers to the fraction of neutrino interactions that are successfully detected and resolution refers to the finite precision with which neutrino energy, direction, and flavor are inferred (i.e., reconstructed) from the measured signals.

The dominant detectable signatures in neutrino experiments arise from $\nu_e/\bar{\nu}_e$ and $\nu_\mu/\bar{\nu}_\mu$ CC interactions. Electrons/positrons (the electron's antiparticle) emerging from $\nu_e/\bar{\nu}_e$ CC interactions generate event topologies (or signatures) that are qualitatively different from those induced by muons/anti-muons generated in $\nu_\mu/\bar{\nu}_\mu$ CC interactions. Furthermore, most next-generation detectors are not designed to distinguish between neutrinos and antineutrinos on an event-by-event basis. Therefore, in a first simplification, neutrino events in this work are classified into ν_μ-like and ν_e-like topologies.

Reconstruction algorithms in neutrino detectors exploit the spatial and temporal patterns of signals recorded by sensors to infer the event topology (ν_μ-like or ν_e-like), as well as the neutrino energy and arrival direction (step (d) in Fig. 2). Their performance is limited by detector properties such as the number, density, and efficiency of detector elements, which determine the instrument's detection efficiency, its energy and angular resolutions, and its accuracy of topology classification. Combining steps (a)–(d) in Fig. 2 yields the synthetic data $\mathbf{u}$, corresponding to the expected number of detected events in a given detector (see Appendix B.4 for the implementation in this work). Fig. 5b shows the distribution of ν_μ-like events after 10 years of measurements with the KM3NeT/ORCA water Cherenkov detector, a 3D array of photosensors currently being deployed deep in the Mediterranean Sea, which will cover a total instrumented volume of approximately $6.7 \times 10^6 \text{m}^3$ once completed. Together with the corresponding distribution of ν_e-like events in $(E_\nu, \cos\theta_z)$, these distributions define the synthetic data $\mathbf{u}$ for KM3NeT/ORCA. Owing to the finite energy and angular resolution of the detector, the oscillation patterns in the interacting-event distribution are smeared out, reducing the contrast of the underlying features.

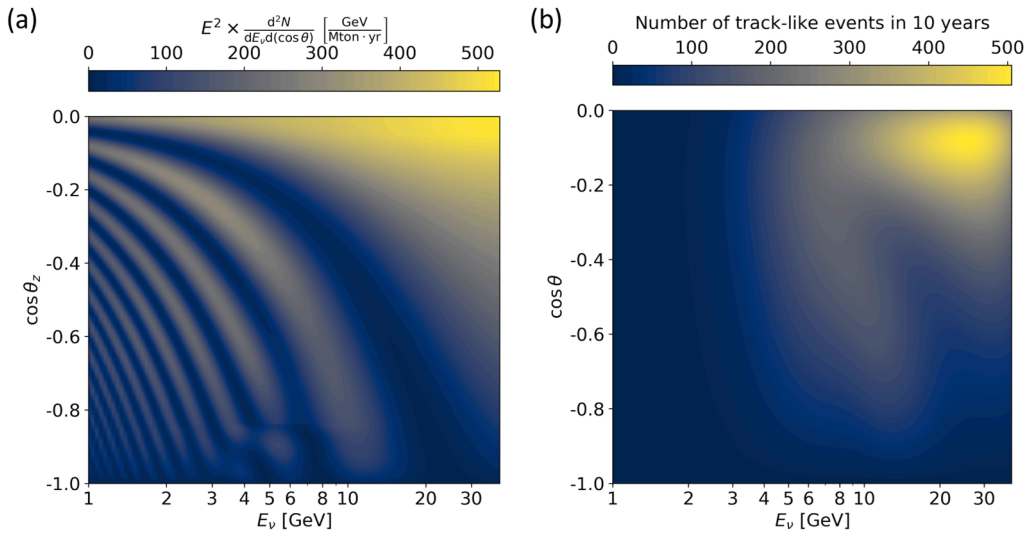


Fig. 5. (a) Simulated rate of interacting neutrinos in the $(\nu_\mu + \bar{\nu}_\mu)$ CC channels (corresponding to 1 Mton-year of exposure of a water-based detector), and multiplied by E_ν^2 to visually compensate for the rapid decrease of the neutrino flux with energy. (b) Expected number of detected ν_μ-like events in a KM3NeT/ORCA-like detector with 10 years of measurements.

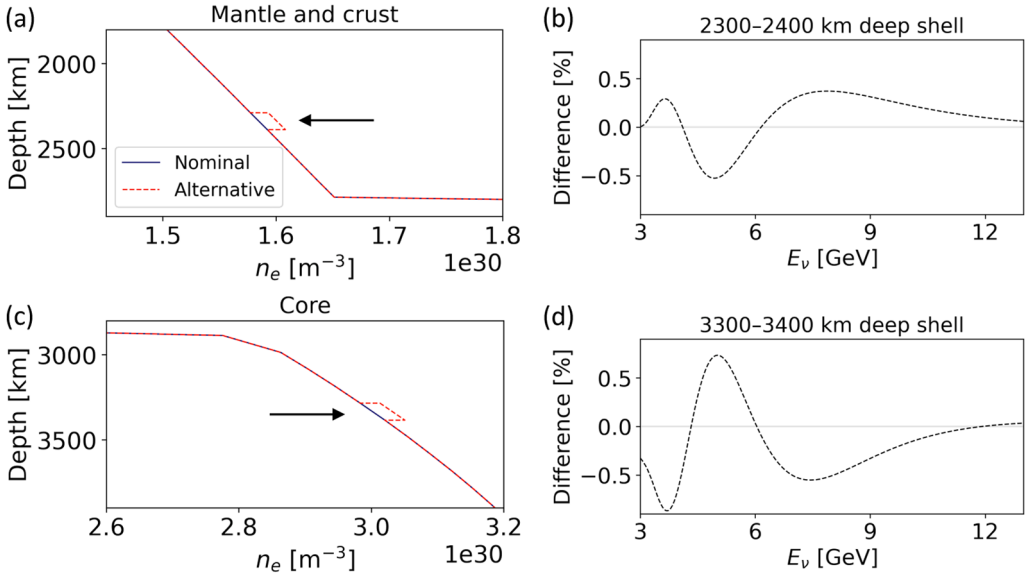


Fig. 6. Electron density profile of the (a) mantle and crust and of the (c) core, (see Section 3.2, solid blue line). In (a), the red dashed curve shows the alternative Earth model in which the electron density is increased only between ~ 2300 km and ~ 2400 km. In (c), the same modification is applied between ~ 3300 km and ~ 3400 km. Panels (b) and (d) show the corresponding differences (in %) in $P_{\nu_e \to \nu_\mu}$ between the nominal and modified Earth models from (a) and (c), respectively. In each case, only neutrinos traversing the modified shell tangentially are considered.

4. Methods

4.1. Forward model setup

For the present work, we employ the EarthProbe framework (Maderer et al., 2023a), which implements the full forward modeling of neutrino observables described in Section 3. Within this framework, several input parameters must be provided.

First, EarthProbe requires an electron density profile, n_e (see Eqs. (8)–(12)). Here, it allows for user-defined ρ and Y_e profiles. In this work, they are discretized into 64 shells. Given the early stage of neutrino oscillation tomography of the Earth (NOTE), we adopt this relatively coarse parameterization of the n_e profile as a first step, although it can be refined in future applications. The nominal Earth model (defined in Section 3.2) is taken to generate the "true" data **d**, while synthetic data **u** are produced using alternative Earth models. The alternative Earth models considered here differ from the nominal one only by a specified percentage in n_e within one of the 64 shells. We verified that the sensitivity scales linearly with the perturbation amplitude (see Appendix B.5), and therefore, without loss of generality, we present results for a +1% modification of n_e.

Moreover, EarthProbe allows for different detector configurations. Each neutrino detector yields corresponding synthetic data **u**, reflecting differences in detector response and reconstruction performance (steps (c) and (d) in Fig. 2). The reconstruction of neutrino properties in EarthProbe follows the paradigm of water Cherenkov detectors such as KM3NeT/ORCA, as it assumes a water detection medium. EarthProbe models the detector response using a set of analytical parameterizations. This approach is sufficiently flexible to emulate technologies beyond water Cherenkov detectors.

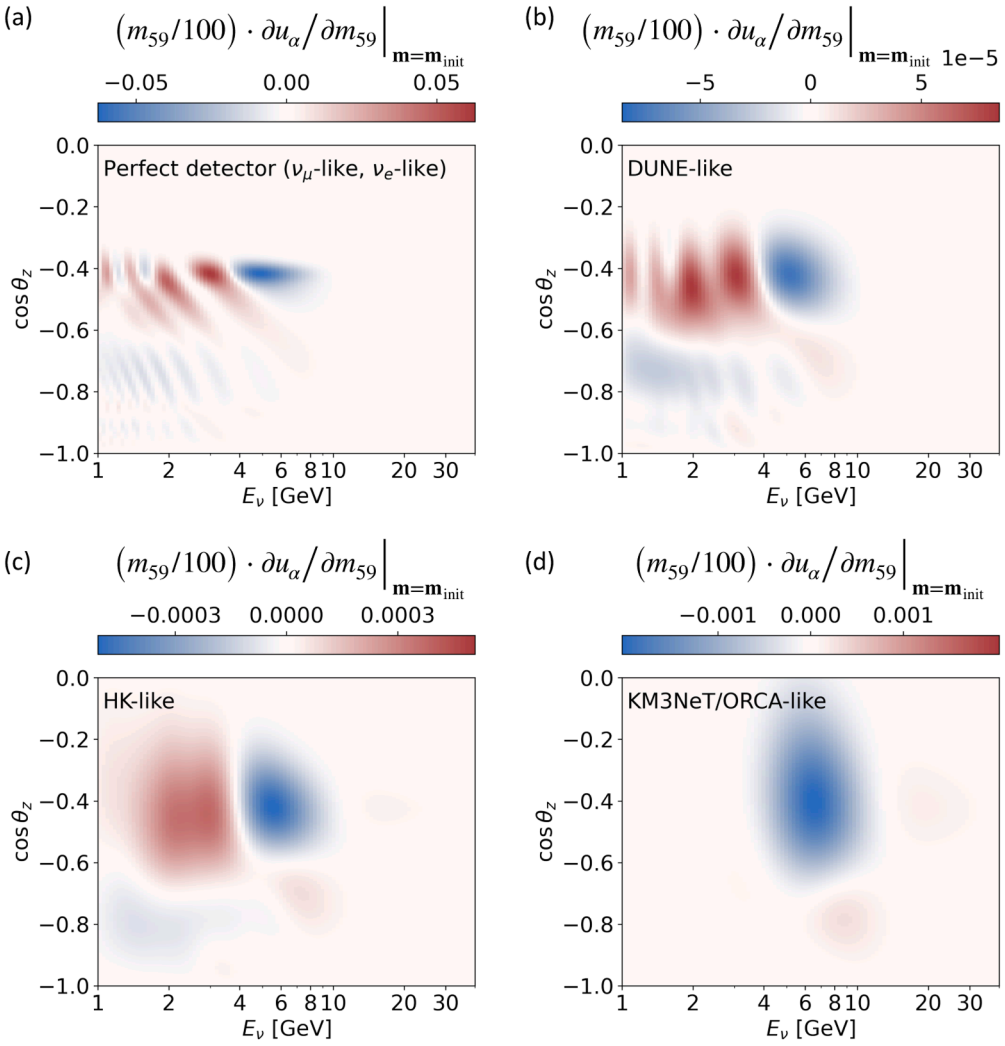


Fig. 7. Fréchet derivatives $\partial u_\alpha / \partial m_i\big|_{\mathbf{m}=\mathbf{m}_{\text{init}}}$ in the inversion for electron density, with the perturbation applied as a percentage variation and normalized to m_{59}. The results are shown for a ∼ 100 km-thick shell within the MTZ, spanning depths from 500 km to 600 km and parameterized by m_{59}. Results are shown for ν_μ-like events in the perfect (a), DUNE-like (b), HK-like (c), and KM3NeT/ORCA-like (d) detectors. The derivatives correspond to a +1% perturbation in electron density.

Regarding the state-of-the-art detectors considered, we use the benchmark parameterizations of KM3NeT/ORCA, Hyper-Kamiokande (Abe et al., 2018), and DUNE (Abi et al., 2020), as provided in Maderer et al. (2023b). Since the parameterizations for KM3NeT/ORCA may evolve as its development progresses, and because HK and DUNE rely on a different detection technology than KM3NeT/ORCA, we refer to these configurations as KM3NeT/ORCA-like, HK-like, and DUNE-like, respectively.

To assess the intrinsic sensitivity of NOTE to perturbations in the Earth model, we also consider an idealized hypothetical detector with near-perfect reconstruction capabilities, referred to hereafter as perfect detector, since its performance is taken to reach the fundamental limits imposed by the underlying detection physics. The corresponding assumptions on efficiency, energy and angular resolution are detailed in Appendix B.4. We further assume that this detector can perfectly identify all eight interaction channels introduced in Section 3.3. Since such channel-identification performance lies beyond the reach of currently funded technologies, we also consider a more realistic configuration in which only ν_μ-like and ν_e-like topologies can be distinguished, while retaining the same assumptions on efficiency and resolution.

Finally, we specify the energy range and binning scheme used for **u** and **d**. For all detector configurations, we use 100 logarithmically spaced energy bins between 1 GeV and 40 GeV, and 800 bins in $\cos\theta_z$ spanning from −1 to 0. Although the sensitivity of NOTE is concentrated roughly between 1 GeV and 11 GeV, we extend the energy range to 40 GeV. This choice is motivated by the limited energy and angular resolution of detectors such as KM3NeT/ORCA, which shifts sensitivity toward higher energies. For HK and DUNE, the contribution to the total sensitivity above 11 GeV is below 0.1%. Thus, including this extended range has no significant impact on the results, while ensuring consistency across detector models. The contribution from energies below 1 GeV is negligible for all detectors. Given our assumption of a 20 year data-acquisition period, we adopt this fine binning in both energy and $\cos\theta_z$, which results in small statistical fluctuations in each bin.

4.2. Toward the inversion of neutrino data

The forward modeling of NOTE can be written in general form (Virieux and Operto, 2010) as

$$\mathbf{u} = \mathcal{G}(\mathbf{m}). \tag{13}$$

Here, **m** denotes the set of Earth model parameters, representing the electron density profile (Section 3.2). In the present work, **m** is a vector with 64 entries (Section 4.1). For a given neutrino detector, the synthetic data **u** consists of event counts binned in energy and incidence angle, and further separated by event topology. The binning scheme adopted

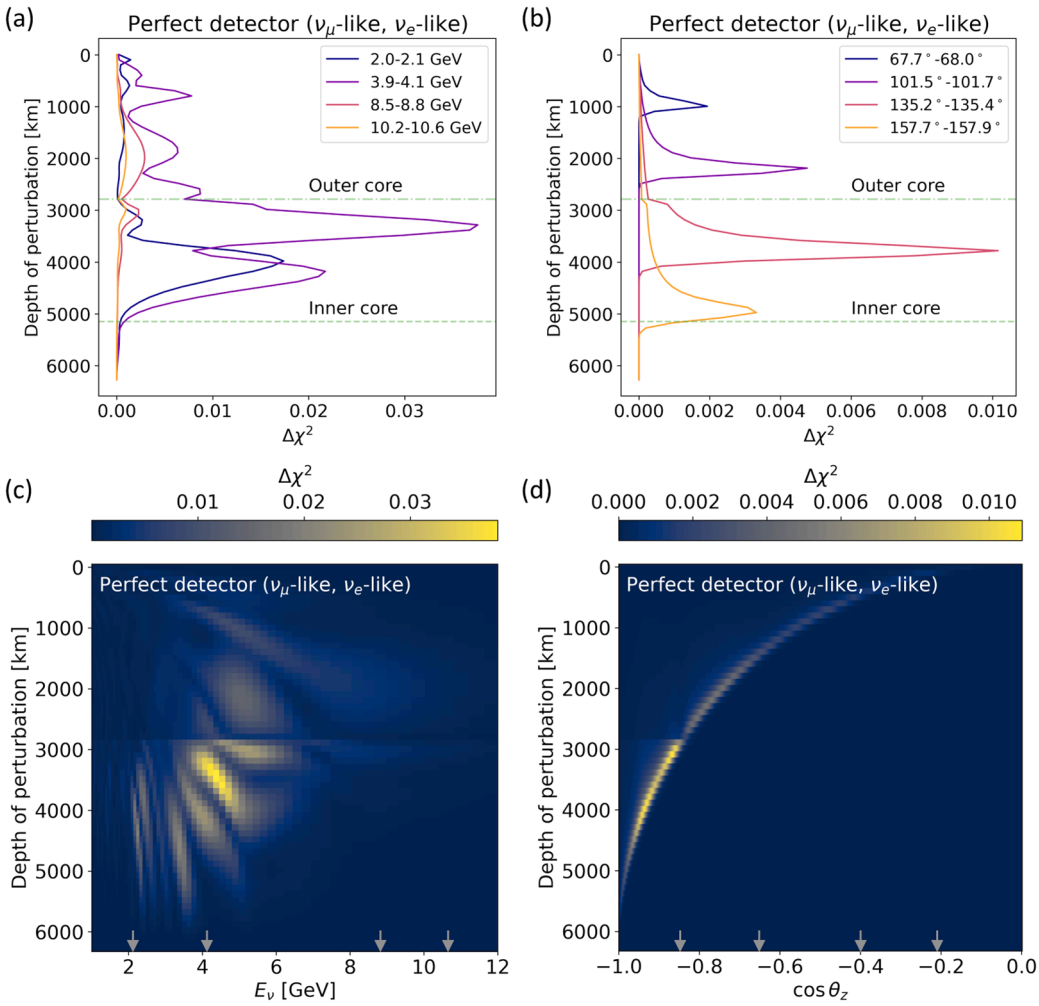


Fig. 8. Sensitivity curves, as defined in Eq. (16), for +1% perturbations in electron density within 100 km-thick shells at different depths. Panels (a) and (c) show the energy dependence for selected energies and for all energies, respectively, while panels (b) and (d) show the corresponding incidence-angle dependence for selected angles and for all angles. The gray arrows in panels (c) and (d) indicate the selected energies shown in (a) and the selected incidence angles shown in (b), respectively. For guidance, the boundaries of the outer core and inner core are also shown in panels (a) and (b).

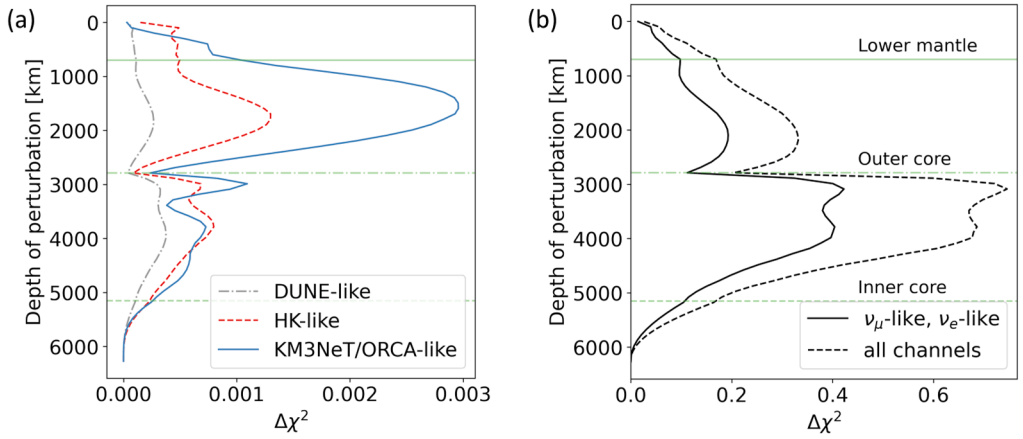


Fig. 9. Total sensitivity curves, as defined in Eq. (16), for +1% electron density perturbations in 100 km-thick shells at different depths. The results for the next-generation detectors DUNE-like, HK-like, and KM3NeT/ORCA-like are shown in (a). A data-acquisition period of 20 years is assumed for all cases, corresponding to exposures of 0.8, 8, and 160 Mton-years, respectively, reflecting the different detector sizes (0.04, 0.4, and 8 Mton, respectively). The intrinsic sensitivity is illustrated in (b) using the perfect detector capable of distinguishing all eight neutrino interaction channels (dashed curve). A more realistic scenario is also shown (solid curve), resorting to the perfect detector distinguishing only two event topologies. In these two cases an exposure of 200 Mton-years is assumed. For guidance, the boundaries of the lower mantle, outer core, and inner core are also shown.

in this work is specified in Section 4.1. Formulating the inverse problem requires knowledge of the inverse of $\mathcal{G}$, which is generally not accessible.

One way to proceed is to linearize the forward problem around the initial Earth model $\mathbf{m}_{\text{init}}$, which is taken to be the nominal Earth model defined in Section 3.2, yielding

$$\mathcal{G}(\mathbf{m}_{\text{init}} + \Delta\mathbf{m}) \simeq \mathcal{G}(\mathbf{m}_{\text{init}}) + \left(\nabla_{\mathbf{m}}\,\mathcal{G}(\mathbf{m})|_{\mathbf{m}=\mathbf{m}_{\text{init}}}\right) \cdot \Delta\mathbf{m}, \tag{14}$$

where $\nabla_{\mathbf{m}}\mathcal{G}(\mathbf{m})$ are the Fréchet derivatives

$$\left[\nabla_{\mathbf{m}}\mathcal{G}(\mathbf{m})\right]_{\alpha i} = \left.\frac{\partial u_\alpha}{\partial m_i}\right|_{\mathbf{m}=\mathbf{m}_{\text{init}}}. \tag{15}$$

This matrix encodes the linear response of the observables to perturbations in the model parameters and therefore constitutes the central ingredient for inversion based on neutrino data. Performing an inversion with neutrinos thus requires the construction of $\nabla_{\mathbf{m}}\mathcal{G}(\mathbf{m})$, a subset of which we present in Section 5.1.

In this work, $\mathbf{m}$ is a 1D parameterization of the Earth. In seismology, such a parameterization is typically used for global or regional 1D inversion, since seismic waves sample extended volumetric regions between source and receiver. In contrast, neutrino rays are straight lines, intersecting a spherically symmetric shell under study at up to two points (one in the tangential case). Consequently, in NOTE, the Fréchet derivatives $\partial u_\alpha/\partial m_i|_{\mathbf{m}=\mathbf{m}_{\text{init}}}$ can be interpreted as encoding sensitivity to localized 3D voxels along the ray. A 3D inversion would require resolving the degeneracy between the two voxels located at the same radial distance from the Earth's center along a given neutrino ray. This step is beyond the scope of this work, but could be addressed by introducing a hemispherical partition of the Earth relative to the detector position. We present Fréchet derivatives that do not account for this distinction.

4.3. Statistical approach to NOTE

Fréchet derivatives constitute the tool for performing inversion. Inspecting them can offer qualitative insight into which regions in $(E_\nu, \cos\theta_z)$ carry stronger predictive power, by identifying energies and incidence angles where $\partial u_\alpha/\partial m_i|_{\mathbf{m}=\mathbf{m}_{\text{i}}}$ is large. However, this interpretation remains only indicative. A large variation in $\mathbf{u}$ in a given bin does not necessarily imply a significant contribution if the corresponding event count has large uncertainty. A quantitative assessment requires accounting for the statistical uncertainty associated with the bin populations.

Consequently, as a measure of the sensitivity of the idealized and realistic next-generation detectors described in Section 4.1 to distinguish two different electron density scenarios, we report in Sections 5.2 and 5.3 the total $\Delta\chi^2$, computed as

$$\Delta\chi^2(\mathbf{m}_{\text{init}}, \mathbf{m}_{\text{mod,i}}) = \sum_{j=1}^{n_E}\sum_{k=1}^{n_\theta} \frac{\left(N_{j,k}^{\text{init}} - N_{j,k}^{\text{mod,i}}\right)^2}{N_{j,k}^{\text{init}}}, \tag{16}$$

where the summation is over the chosen number of n_E energy and n_θ incidence angle bins. $\mathbf{m}_{\text{mod,i}} = \mathbf{m}_{\text{init}} + \Delta\mathbf{m}$ refers to the alternative Earth model, that differs from the nominal one by a modification of n_e in the ith shell. $N_{j,k}^{\text{init}}$ and $N_{j,k}^{\text{mod,i}}$ denote the numbers of detected neutrino events for the initial and modified Earth models, respectively, and follow Poisson statistics. The binning described in Section 4.1 is sufficiently fine to approximate the limit of infinitely small bins. The values $\Delta\chi^2(\mathbf{m}_{\text{init}}, \mathbf{m}_{\text{mod,i}})$ should be interpreted as the statistical significance with which the nominal model would be rejected if the event counts $N_{j,k}^{\text{mod,i}}$ in Eq. (16) were observed.

4.4. Physical origin of the sensitivity of NOTE

The sensitivity of NOTE depends on how strongly variations in the Earth model affect the neutrino rates. The model parameters $\mathbf{m}$ directly influence the neutrino oscillation probabilities, which modulate the flavor composition of the atmospheric neutrino flux traversing the Earth and thereby translate into changes in the observed neutrino rates across flavors.

In the simplified case of a uniform Earth with constant electron density n_e^0, oscillation probabilities are proportional to $\sin^2\left(c(n_e^0)\cdot L/E_\nu\right)$, where L is the propagation distance and $c(n_e^0)$ is a constant that depends on the electron density. For specific combinations of L and E_ν, this term varies strongly between Earth models, leading to large changes in oscillation probabilities, thus neutrino rates, and therefore increased sensitivity. These conditions correspond to resonant oscillations, known as MSW resonances (for Mikheyev, Smirnov, and Wolfenstein). In the Earth, such resonances occur for neutrinos with ~ 3 GeV traversing the outer core and with ~ 7 GeV traversing the mantle.

Neutrino flavor oscillations within the Earth can undergo another form of resonant enhancement, known as parametric resonance, arising from density transitions between different terrestrial layers (Chizhov et al., 1998; Akhmedov, 1999). In this case, effects accumulated in successive regions can combine in a constructive manner, leading to a significant modification of the final oscillation probability and increased sensitivity.

The interplay of both resonance mechanisms gives rise to energy ranges in which neutrinos traversing specific regions of the Earth undergo enhanced modifications of their oscillation probabilities. Fig. 6 illustrates the effect of increasing by 1% the electron density in a shell located either in the mantle (6a-b) or in the core (6c-d) on the oscillation probability $P_{\nu_e\to\nu_\mu}$, for neutrinos propagating tangentially through each shell. In the core, a variation in electron density could reflect differences in light-element alloy composition, such as FeH versus FeX (with X≠H). The deviation between the nominal and modified Earth models is generally larger (in absolute value) when the perturbation is located in the core.

5. Sensitivity of NOTE to variations in the radial electron density

5.1. Fréchet derivatives

In this section, we present a subset of the Fréchet derivatives introduced in Section 4.2 that form the basis of a future linearized inversion. Fig. 7 shows these derivatives with respect to a density change in a ~ 100 km-thick shell within the mantle transition zone (MTZ). The corresponding Fréchet derivatives are shown for the detector configurations used in this work, across all energy and incidence-angle bins, and restricted to ν_μ-like events. In NOTE, Fréchet derivatives depend on energy, incidence angle, and flavor (encoded through event topologies). Furthermore, as required for the linearized inversion, they are linear in the perturbation amplitude (see Appendix B.5).

For the perfect detector, $\partial u_\alpha/\partial m_i\big|_{\mathbf{m}=\mathbf{m}_{\text{init}}}$ vanishes above 500 km, since neutrinos that do not cross the 500 km–600 km shell are unaffected. The largest values occur for neutrinos crossing this shell tangentially (at $\cos\theta_z \simeq -0.4$, or equivalently $\Delta \simeq 48°$), which maximizes their path length through the perturbed region. For more vertical rays, the shell is crossed twice but over shorter path lengths, reducing the effect. In the DUNE-like detector, finite energy and angular resolutions induce event migration between bins, in particular into angular bins above the perturbed shell, and leading to a smearing of the pattern observed in Fig. 7b. This effect becomes progressively stronger for the HK-like and KM3NeT/ORCA-like configurations, whose resolutions are comparatively poorer.

Additionally, the range of $\partial u_\alpha/\partial m_i\big|_{\mathbf{m}=\mathbf{m}_{\text{init}}}$ values varies across detectors, increasing with detector size. Consequently, for the KM3NeT/ORCA-like configuration, although the fine structure of the pattern from Fig. 7a is degraded by limited resolution, the residual signal remains sufficiently strong to make such a detector potentially relevant for NOTE.

5.2. Sensitivity dependence on energy and incidence angle

In this section and the next, we assess the sensitivity of NOTE to perturbations in individual shells, as described in Section 4.3. To assess the energy and angular dependence of NOTE sensitivity in a perfect detector, we use Eq. (16), first summing over all $n_\theta = 800$ incidence-angle bins considered in this work while retaining a single energy bin ($n_E = 1$, Fig. 8a and c) and second summing over all $n_E = 100$ energy bins while retaining a single incidence-angle bin ($n_\theta = 1$, Fig. 8b and d). Each depth on the y-axis corresponds to the comparison between neutrino rates computed with the nominal Earth model and an alternative model $\mathbf{m}_{\text{mod,i}}$, while the x-axis shows the computed $\Delta\chi^2$ values.

We find that the sensitivity for neutrinos with energies around 4 GeV is highest to perturbations in the outer core (Fig. 8a and c). This behavior is driven by the MSW resonance experienced by low-energy neutrinos traversing it. The MSW resonance around 7 GeV in the mantle enhances the sensitivity to mantle perturbations for neutrinos of higher energy, while NOTE sensitivity becomes negligible for neutrino energies above ~ 11 GeV.

Neutrinos in a narrow incidence-angle bin are most sensitive to perturbations of the shell they cross tangentially (Fig. 8b and d). If the perturbed shell is deeper and not traversed, the contribution vanishes, and if it is shallower and crossed twice over short paths, $\Delta\chi^2$ is small but non-zero. As a result, the sensitivity curves peak at the depth corresponding to tangential crossing. The peak heights reflect the combined contribution of all energies.

5.3. Total sensitivity

Finally, we examine the total sensitivity to +1% electron density perturbations in 100 km-thick shells by summing over all $n_E = 100$ energy and $n_\theta = 800$ incidence-angle bins (Fig. 9). These sensitivity curves demonstrate the impact of including NOTE in an inversion framework as well as the performance of next-generation detectors (Fig. 9a) relative to a perfect detector (Fig. 9b), thereby indicating where improvements in experimental performance would most effectively enhance sensitivity.

Each sensitivity curve in Fig. 9a can be loosely (as systematic uncertainties are not included) interpreted as a lower bound on sensitivity for the corresponding next-generation detector due to the following. A 1% increase in electron density within a shell represents a local perturbation that is not physically self-consistent, as it violates hydrostatic equilibrium (HE). In a realistic scenario, such a change would require correlated adjustments in the surrounding structure to preserve the Earth's total mass, moment of inertia, and HE. These coupled modifications would lead to a larger deviation from the nominal model, resulting in stronger changes in neutrino event rates and thus enhanced sensitivity.

In contrast, the dashed curve in Fig. 9b, corresponding to the perfect detector capable of distinguishing all eight neutrino interaction channels, represents an upper bound and can be interpreted as the intrinsic sensitivity of NOTE to these perturbations. The solid curve corresponds to a more realistic perfect detector distinguishing only two event topologies. In both cases, the sensitivity to increases in electron density is highest in the Earth's outer core. It decreases sharply toward the Earth's center due to the reduced number of neutrinos probing progressively smaller shells and the shorter path lengths through them. Sensitivity in the mantle is significantly lower, mainly because lower-density shells correspond to higher resonance energies where the atmospheric neutrino flux is reduced.

The gap between the sensitivity of next-generation detectors and the idealized case reflects limitations in event reconstruction. The reduction in sensitivity is larger in the core because neutrinos traversing it experience MSW resonances near 3 GeV, compared to ~ 7 GeV for mantle-crossing neutrinos, and reconstruction performance degrades at lower energies for all detectors. The effect is largest for KM3NeT/ORCA, intermediate for HK, and smallest for DUNE, reflecting their respective resolutions and efficiencies (Maderer et al., 2023b).

6. Conclusions

Research on the Earth's internal structure has advanced greatly over the past century, yet key questions remain, such as the precise density and hydrogen content of different regions, motivating the search for new observables that complement traditional geophysical methods. One promising observable is the flux of atmospheric neutrinos traversing the Earth, whose oscillation patterns carry information about the electron density along their rays. In this paper, we take a step toward integrating neutrino oscillation measurements into a joint inversion framework with seismic data by describing the forward problem, formulating its linearization, and quantifying the sensitivity of the associated Fréchet derivatives to perturbations in the Earth's electron density profile.

We first describe the forward modeling of neutrino oscillation tomography of the Earth (NOTE). We then demonstrate that the Fréchet derivatives required for the linearized inverse problem can be computed and that they scale linearly with the amplitude of perturbations in electron density. This is done for expected neutrino rates at the next-generation KM3NeT/ORCA detector, which is under construction and steadily accumulating data, as well as for HK and DUNE, which are scheduled to begin data acquisition in the coming years. We also consider an idealized hypothetical detector to assess the intrinsic sensitivity of the method.

To investigate the sensitivity of the Fréchet derivatives to localized perturbations, we study the response of neutrino oscillations to a 1% increase in electron density within ~ 100 km-thick shells. To approximate the intrinsic sensitivity, we consider the idealized detector representing the fundamental performance limit. While this idealized detector shows the highest sensitivity to perturbations in the core, realistic detectors exhibit overall reduced sensitivity that shifts toward the mantle. Thus, detector performance plays an important role in determining which regions of the Earth can be probed most effectively. The sensitivity decrease arises from reduced detection efficiency and finite energy and angular resolution and is more pronounced at lower energies, where MSW resonances occur for core-traversing neutrinos. Future work should identify which detector characteristics most effectively enhance sensitivity to different Earth regions, thereby guiding the design of next-generation instruments.

These results establish the basis for developing a joint inversion framework combining seismic data and neutrino oscillation tomography of the Earth, with the latter providing constraints on the Earth's electron density distribution. Such constraints on electron density could help test specific geochemical hypotheses, such as localized hydrogen enrichment or proposed heavy-element concentrations. In its most complete form, such a framework would integrate neutrino observations from multiple detectors as well as neutrino absorption tomography, providing more comprehensive and complementary constraints on the Earth's internal structure.

CRediT authorship contribution statement

Isabel A. Goos: Writing – original draft, Methodology, Investigation, Formal analysis, Conceptualization; **Nobuaki Fuji:** Writing – original draft, Supervision, Investigation, Funding acquisition, Conceptualization; **Stéphanie Durand:** Writing – original draft, Validation, Investigation, Conceptualization; **Véronique Van Elewyck:** Writing – review &

editing, Supervision, Methodology, Investigation, Funding acquisition, Conceptualization; **João A. B. Coelho:** Writing – review & editing, Supervision, Methodology, Investigation, Conceptualization; **Eric Mittelstaedt:** Writing – review & editing, Validation, Methodology, Investigation, Conceptualization; **Yael Deniz:** Writing – original draft, Validation, Methodology, Investigation, Conceptualization.

Ethics declaration

The author(s) declare(s) that the study does not involve humans nor animal subjects.

Declaration of competing interest

The author(s) declare(s) that the study does not have competing interests.

Acknowledgements

We would like to express our sincere gratitude to the editor and the reviewers for their insightful comments, constructive feedback, and helpful suggestions. João A. B. Coelho, Nobuaki Fuji, Isabel Goos and Véronique Van Elewyck were supported by the program "Investissement d'Avenir", launched by the French Government and implemented by ANR (ANR-21-EXES-0002, Fire-UP Program "Crossing Cutting Edges" and InIdex project HERMES "Multi-messengers of the Earth and the Universe"). Nobuaki Fuji was supported by the Institut Universitaire de France. Eric Mittelstaedt and Yael Deniz were supported by the award 2406115 from the United States National Science Foundation.

Data availability

No data was used for the research described in the article.

Appendix A. Physical constants, variables, and expressions

In this appendix, we provide tables listing the physical constants, variables, and expressions used in this study (Tables A.1–A.5).

Table A.1
Table of physical constants used in this study and their values. The neutrino oscillation parameters (Θ_{ij}, Δm^2_{ij}, and δ_{CP}) are taken from Esteban et al. (2025). Other constants are taken from Olive et al. (2014).

Symbol	Description	Value
Θ_{12}	"solar" mixing angle	33.68°
Θ_{13}	"reactor" mixing angle	8.56°
Θ_{23}	"atmospheric" mixing angle	43.3°
Δm^2_{21}	"solar" mass-squared difference	$7.49 \times 10^{-5}\mathrm{eV}^2$
Δm^2_{31}	"atmospheric" mass-squared difference	$2.513 \times 10^{-3}\mathrm{eV}^2$
δ_{CP}	CP-violating phase	212°
M_{u}	molar mass constant	1 g mol^{-1}
$\mathcal{N}_{\mathrm{A}}$	Avogadro number	$6.022140857 \times 10^{23}$ mol^{-1}
$\hbar c$	reduced Planck constant × speed of light	$1.973269788 \times 10^{-10}$ eV km
G_{F}	Fermi constant	1.1663787×10^{-5} GeV^{-2}

Table A.2
Table of variables used in this study and their units.

Symbol	Description	Unit
E_ν	neutrino energy	GeV
θ_z	neutrino zenith angle	dimensionless
Δ	epicentral distance	°
t, T	travel time of the neutrino within the Earth	s
L	path length	km
n_e	electron density	m^{-3}
ρ	matter density	kg m^{-3}
Y_e	electron yield	dimensionless
Z	atomic number	dimensionless
A	standard atomic weight	dimensionless
w	weight fraction	dimensionless
ϕ_ν	flux of atmospheric neutrinos	$(\mathrm{cm}^2\ \mathrm{s\ sr\ GeV})^{-1}$
Mw	moment magnitude scale	dimensionless

Table A.3
Values of electron yield used in this work.

Layer	Radial extent [km]	Electron yield Y_e
Sea	6368.0 – 6371.0	0.5524
Crust	6346.6 – 6368.0	0.4956
Mantle	3480.0 – 6346.6	0.4954
Core	0 – 3480.0	0.4691

Table A.4
Expressions used in this study and their meaning.

Symbol	Description
ν_e, $\bar{\nu}_e$	electron neutrino, electron antineutrino
ν_μ, $\bar{\nu}_\mu$	muon neutrino, muon antineutrino
ν_τ, $\bar{\nu}_\tau$	tau neutrino, tau antineutrino
$\nu/\bar{\nu}$	generic neutrino/antineutrino, if the flavor doesn't matter
ν_X	representative of any of the eight neutrino interaction channels
α, β	reserved for flavor e, μ, or τ
α^-/α^+	reserved for particle e, μ, or τ/ antiparticle of e, μ, or τ
$\nu_\alpha \to \nu_\beta$	oscillation process from ν_α to ν_β
$\mathrm{P}_{\nu_\alpha \to \nu_\beta}$	probability of the oscillation process from ν_α to ν_β
$\lvert\nu_\alpha\rangle$	neutrino flavor eigenstates
$\lvert\nu_i\rangle$, $i \in \{1,2,3\}$	neutrino mass eigenstates
m_i, $i \in \{1,2,3\}$	neutrino masses
$\mathcal{H}$	Hamiltonian governing the system's evolution
$\mathcal{H}_{\mathrm{vacuum}}$	Hamiltonian in vacuum
$\mathcal{H}_{\mathrm{matter}}$	effective matter Hamiltonian
V_e	matter-induced potential
$\vec{x}$	position in space
$\vec{x}_{\mathrm{entry}}$	position where a neutrino enters the Earth
NC/CC	neutral-current/charged-current (interaction)
Z^0, $W^\pm$	weak-force bosons
ν_μ/ν_e-like	event topologies
$\mathcal{G}$	function encoding the forward modeling
$\mathbf{m}$	Earth model parameters, with elements m_i
$\mathbf{u}$	synthetic data, with elements u_α
$\mathbf{d}$	real data
$\nabla_{\mathbf{m}}\mathcal{G}(\mathbf{m})$	Fréchet derivatives
$\mathbf{m}_{\mathrm{init}}$	nominal or initial Earth model
$\mathbf{m}_{\mathrm{mod,i}}$	alternative Earth model where the ith shell was modified
$\Delta\mathbf{m}$	$= \mathbf{m}_{\mathrm{mod,i}} - \mathbf{m}_{\mathrm{init}}$

Table A.5
Continuation of Table A.4.

Symbol	Description
$\Delta\chi^2$	test statistic defined in Eq. (16)
n_E/n_θ	number of energy bins/incidence-angle bins
$N^{\text{init}}_{j,k}/N^{\text{mod,i}}_{j,k}$	number of detected neutrino events for the initial/modified Earth model
$\mathcal{T}$	time-ordering operator
Δt_k, t_k	time intervals, intermediate values
$N^{\text{int}}_{\nu_X}/R^{\text{int}}_{\nu_X}$	number/rate of interacting neutrino events
$T_{\text{det}}/M_{\text{det}}$	data-acquisition time/mass of a neutrino detector
$\sigma^{\text{int}}_{\nu_X}$	cross section of neutrino interaction ν_X
m_{N}	average mass of target nucleons in a medium
$\sigma(E_\nu)$	smearing function representing energy resolution
$\sigma(\theta_z; E_\nu)$	smearing function representing angular resolution
$\epsilon_{\text{det}}(E_\nu)$	efficiency of successful detection
$\epsilon_{\text{class}}(E_\nu)$	efficiency of successful classification
n^0_e	particular constant value of electron density
$c(n^0_e)$	constant expression that depends on n^0_e
Ψ	variable expression that depends on m_j, E_ν, and L

Appendix B. Details of neutrino oscillation probability calculations

This appendix presents additional technical material on the modeling of neutrino observables, for which we employ the EarthProbe framework (Maderer et al., 2023a).

B.1. Atmospheric neutrino flux configuration

This appendix provides the specific atmospheric neutrino flux configuration used in the present study.

In this work, we use the benchmark atmospheric neutrino flux computed for the Gran Sasso site (no mountain overburden), averaged over azimuth and seasonal variations, and assuming minimum solar activity (Hon, 2026). Gran Sasso, which hosts the underground laboratory (Lng, 2026), lies at a latitude similar to that of the detectors considered here. Flux differences between these sites are expected to be within $\sim 1\%$ (Honda et al., 2015). Averaging over seasons is appropriate, as NOTE will rely on data collected over several years. Solar activity modulates the flux of low-energy cosmic rays entering the atmosphere, thereby affecting the production of atmospheric neutrinos. This effect remains below 1% for neutrino energies above 3 GeV and reaches at most 3% at lower energies (Honda et al., 2015). The overall neutrino flux has an estimated systematic uncertainty of 7% below 10 GeV, and 14% in the range between 10 GeV and 100 GeV.

B.2. Implementation of neutrino oscillations

This appendix specifies the parameters entering $\mathcal{H}_{\text{vacuum}}$ and outlines the solution of the Schrödinger equation for neutrino oscillations in matter adopted in the present work.

The vacuum Hamiltonian $\mathcal{H}_{\text{vacuum}}$ is fully determined by six parameters: the mixing angles Θ_{12}, Θ_{13}, and Θ_{23}, the mass-squared differences Δm^2_{21} and Δm^2_{31} (with $\Delta m^2_{ij} = m^2_i - m^2_j$), and the complex phase δ_{CP}. We adopt the oscillation parameters from Esteban et al. (2025), based on global fits performed by the NuFIT collaboration and regularly updated with new experimental data. The first four parameters are now known to percent-level precision, whereas δ_{CP} is still poorly constrained and the sign of Δm^2_{31} remains undetermined. Consequently, the neutrino mass ordering, whether $m_1 < m_2 \ll m_3$ (normal ordering) or $m_3 \ll m_1 < m_2$ (inverted ordering), is still unknown. This unknown physical property affects neutrino oscillation probabilities and therefore impacts this study. Throughout our analysis, we assume the normal mass ordering, which is currently slightly favored by global data (Esteban et al., 2025). NOTE requires long data-acquisition periods. By the time sufficient data have been accumulated to probe the deep Earth with neutrinos, all six oscillation parameters are expected to be known with high precision.

To solve the Schrödinger equation in matter for a given neutrino ray, defined by Eqs. (6)–(12), EarthProbe builds a sequence of the Earth matter segments successively traversed by the neutrino, each having constant electron density. The solution is then given by:

$$|\nu_\alpha(T)\rangle = \mathcal{T}\left\{\exp\left(-\frac{i}{\hbar}\int_0^T \mathcal{H}(t')\,dt'\right)\right\}|\nu_\alpha(0)\rangle\,, \tag{B.1}$$

where T is the time the neutrino needs to cross the Earth and $\mathcal{T}$ is the time-ordering operator that ensures computations follow the correct temporal sequence of segment crossings. Note that Eq. (B.1) is the matrix generalization of the solution $\exp(-iE_\nu t/\hbar)\,|\nu(0)\rangle$ of the Schrödinger equation with a time-independent Hamiltonian $\mathcal{H}$ in one dimension, $i\hbar\partial_t\,|\nu(t)\rangle = \mathcal{H}\,|\nu(t)\rangle$.

After discretizing the total time T into small time intervals Δt_k, the OscProb package (Coelho et al., 2023) is used to solve Eq. (B.1) numerically, by approximating $\mathcal{H}(t)$ as a sequence of piecewise-constant Hamiltonians $\mathcal{H}(t_k)$, each defined over the time interval Δt_k:

$$|\nu_\alpha(T)\rangle \approx \mathcal{T}\left\{\prod_k \exp\left(-\frac{i}{\hbar}\,\mathcal{H}(t_k)\,\Delta t_k\right)\right\}|\nu_\alpha(0)\rangle\,. \tag{B.2}$$

Solving Eq. (B.2) finally requires computing the matrix exponential of each 3×3 Hermitian matrix $\mathcal{H}(t_k)$. OscProb performs this operation efficiently by solving the eigensystem of each Hamiltonian using the hybrid algorithm described in Kopp (2008), and computing the singular value decomposition of the symmetric matrix in the first term of Eq. (9).

B.3. Computation of neutrino interaction rates

This appendix describes the computation of neutrino interaction rates in a target volume used in this work, independent of the subsequent detection technique.

As explained in Section 3.3, we consider eight neutrino interaction channels, which are denoted here for simplicity by ν_X. For each channel ν_X, the differential interaction rate with target nucleons is computed as a binned function of energy and zenith angle, per unit exposure (Maderer et al., 2023b):

$$R^{\text{int}}_{\nu_X}\left(E^i_\nu, \cos\theta^j_z\right) \equiv \frac{\mathrm{d}^4 N^{\text{int}}_{\nu_X}\left(E^i_\nu, \cos\theta^j_z\right)}{\mathrm{d}E^i_\nu\,\mathrm{d}\left(\cos\theta^j_z\right)\,\mathrm{d}T_{\text{det}}\,\mathrm{d}M_{\text{det}}}, \tag{B.3}$$

where T_{det} is the data-acquisition time, M_{det} the mass of the instrumented volume, and E^i_ν and $\cos\theta^j_z$ are the centers of the i-th energy bin and the j-th $\cos\theta_z$ bin, respectively. To compute this rate, EarthProbe weighs the atmospheric neutrino flux Φ_{ν_β} by the corresponding probabilities $\mathrm{P}_{\nu_\beta\to\nu_X}$ to oscillate into the flavor associated to channel ν_X or to stay in that flavor, and then multiplies the resulting flux arriving at the detector by the channel-dependent cross section $\sigma^{\text{int}}_{\nu_X}$, which is a measure of the probability that the neutrino undergoes this interaction and is given in units of area (representing the effective target size):

$$R^{\text{int}}_{\nu_X}\left(E^i_\nu, \cos\theta^j_z\right) = \left(\sum_{\beta=e,\mu} \frac{\mathrm{d}^2\Phi_{\nu_\beta}\left(E^i_\nu, \cos\theta^j_z\right)}{\mathrm{d}E^i_\nu\,\mathrm{d}\left(\cos\theta^j_z\right)}\,\mathrm{P}_{\nu_\beta\to\nu_X}\left(E^i_\nu, \cos\theta^j_z\right)\right)\frac{\sigma^{\text{int}}_{\nu_X}\left(E^i_\nu\right)}{m_{\text{N}}}. \tag{B.4}$$

Here, $\nu_\beta \in \{\nu_e, \nu_\mu\}$ ($\nu_\beta \in \{\bar\nu_e, \bar\nu_\mu\}$) when ν_X is a neutrino (antineutrino) channel. The contribution of atmospheric tau (anti)neutrinos is neglected, as they are very rarely produced in extensive air showers. The cross section is divided by the average mass m_{N} of the target nucleons in the medium, so that event rates for a given detector can be obtained by multiplying $R^{\text{int}}_{\nu_X}$ by the detector mass.

Finally, for a given detector exposure $T_{\text{det}}M_{\text{det}}$, the expected number of neutrinos interacting within the detector in a specific energy and

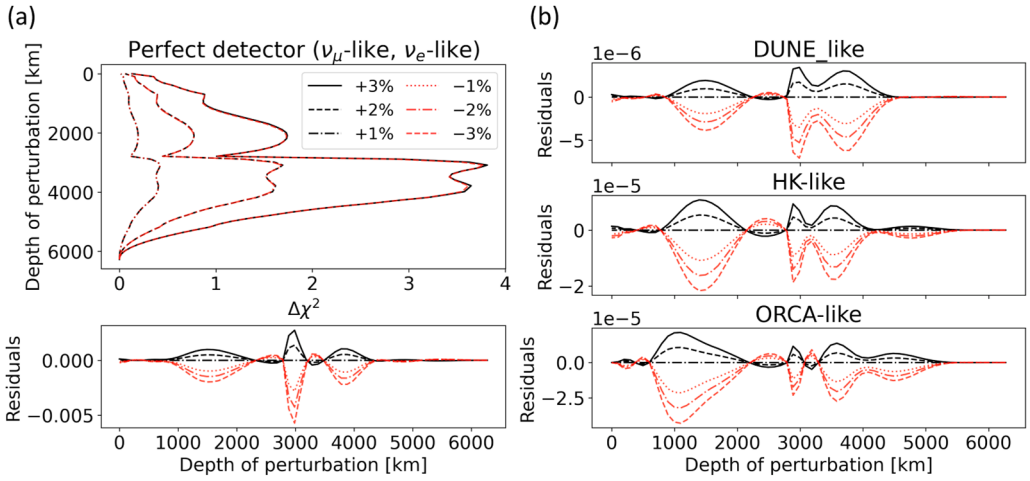


Fig. B.10. The upper panel in (a) shows sensitivity curves for the perfect detector (capable of distinguishing two event topologies) and for ±1%, ±2%, and ±3% perturbations in n_e. The lower panel shows the corresponding residuals obtained by comparing the rescaled sensitivity curves to the +1% reference. The same residual analysis is shown in (b) for the next-generation detectors (DUNE-like, HK-like, and KM3NeT/ORCA-like, from top to bottom).

incidence-angle bin through channel ν_X is computed as:

$$N^{\text{int}}_{\nu_X}\left(E^i_\nu, \cos\theta^j_z\right) = R^{\text{int}}_{\nu_X}\left(E^i_\nu, \cos\theta^j_z\right)\, \Delta E^i_\nu\, \Delta\left(\cos\theta^j_z\right)\, T_{\text{det}}\, M_{\text{det}}. \tag{B.5}$$

B.4. Modeling of neutrino detection

This appendix describes the modeling of the detector response and details the assumptions underlying the idealized detector configuration referred to in the main text as the perfect detector.

To account for detector uncertainties and inefficiencies, EarthProbe employs a set of analytical functions to model the detector response. These consist of smearing functions $\sigma(E_\nu)$ and $\sigma(\theta_z; E_\nu)$, as well as efficiency functions $\epsilon_{\text{det}}(E_\nu)$ and $\epsilon_{\text{class}}(E_\nu)$. The smearing functions encode the resolution of the reconstructed properties (note that the angular resolution is energy dependent), while the efficiency functions describe the probability of successful detection and event classification, respectively. More specifically, $\epsilon_{\text{det}}(E_\nu)$ represents the probability of detecting a neutrino interaction and is taken to be zero below the detector energy threshold, whereas $\epsilon_{\text{class}}(E_\nu)$ gives the probability of correctly assigning an interacting event to its topology (e.g., classifying a ν_μ CC interaction as ν_μ-like). All functions are parameterized with a small number of user-defined parameters (for full details, see Maderer et al., 2023b).

The idealized next-generation detector, referred to in this work as the perfect detector, is used to assess the intrinsic sensitivity of NOTE. It thus represents the limiting case in which all detector effects are reduced to the fundamental irreducible uncertainties associated with neutrino interaction kinematics. The remaining uncertainties on the reconstructed neutrino energy and incidence angle originate solely from the stochastic nature of the interaction kinematics due to nuclear Fermi motion. In this limit, the energy resolution is negligible, while the angular resolution is parametrized as

$$\sigma(\theta_z) = \frac{2.6^\circ}{\sqrt{E_\nu}}. \tag{B.6}$$

The detector is further assumed to achieve full efficiency over the relevant energy range, and a benchmark instrumented mass of 10 Mton is adopted.

B.5. Linearity in the forward modeling

For a linearized inversion, the Fréchet derivatives must scale linearly with the amplitude of the perturbation in the model parameters. In this appendix, we demonstrate this behavior for the sensitivity curves, which differ from the Fréchet derivatives mainly through the squared difference of neutrino rates between nominal and alternative Earth models. The upper panel of Fig. B.10 shows sensitivity curves for the perfect detector and different perturbation amplitudes. We observe that increasing the amplitude from 1% to 2% (3%) leads to an approximate increase by a factor of 2^2 (3^2) of the sensitivity, consistent with the quadratic dependence in the $\Delta\chi^2$ definition. To quantify deviations from this approximation, the lower panel shows the residuals obtained by comparing the rescaled sensitivity curves to the +1% case. We verify that this relation also holds for realistic detectors (Fig. B.10b). These results indicate that perturbations of up to ±3% in n_e remain in the linear regime for NOTE.

References

Abbasi, R., Ackermann, M., Adams, J., Agarwalla, S.K., Aguilar, J.A., Ahlers, M., Alameddine, J.M., Ali, S., Amin, N.M., Andeen, K., et al., 2026. Evidence for a spectral break or curvature in the spectrum of astrophysical neutrinos from 5 tev to 10 pev. Phys. Rev. Lett. 136 (12), 121002.

Abe, K., Abe, K., Aihara, H., Aimi, A., Akutsu, R., Andreopoulos, C., Anghel, I., Anthony, L., Antonova, M., Ashida, Y., et al., 2018. Hyper-kamiokande design report. arXiv:1805.04163

Abi, B., Acciarri, R., Acero, M.A., Adamov, G., Adams, D., Adinolfi, M., Ahmad, Z., Ahmed, J., Alion, T., Monsalve, S.A., et al., 2020. Volume I. Introduction to DUNE. J. Instrum. 15 (08), T08008.

Adrian-Martinez, S., Ageron, M., Aharonian, F., Aiello, S., Albert, A., Ameli, F., Anassontzis, E., Andre, M., Androulakis, G., Anghinolfi, M., et al., 2016. Letter of intent for KM3net 2.0. J. Phys. G: Nucl. Part. Phys. 43 (8), 084001.

Akhmedov, E.K., 1999. Parametric resonance of neutrino oscillations and passage of solar and atmospheric neutrinos through the Earth. Nucl. Phys. B 538 (1–2), 25–51.

Aki, K., Christoffersson, A., Husebye, E.S., 1976. Three-dimensional seismic structure of the lithosphere under montana LASA. Bull. Seismol. Soc. Am. 66 (2), 501–524.

Athar, M.S., Barwick, S.W., Brunner, T., Cao, J., Danilov, M., Inoue, K., Kajita, T., Kowalski, M., Lindner, M., Long, K.R., et al., 2022. Status and perspectives of neutrino physics. Prog. Part. Nucl. Phys. 124, 103947.

Blanco, F., La Rocca, P., Riggi, F., 2009. Cosmic rays with portable Geiger counters: from sea level to airplane cruise altitudes. Eur. J. Phys. 30 (4), 685–695.

Bourret, S., Coelho, J., Van Elewyck, V., 2017. Neutrino oscillation tomography of the Earth with KM3NeT-ORCA. PoS ICRC2017, 1020. https://doi.org/10.22323/1.301.1020

Capozzi, F., Petcov, S.T., 2022. Neutrino tomography of the Earth with ORCA detector. Eur. Phys. J. C 82 (5), 461. 2111.13048. https://doi.org/10.1140/epjc/s10052-022-10399-6

Chattopadhyay, S., Krishnamoorthi, J., Upadhyay, A.K., Collaboration, I., 2025. Demonstrating the ability of icecube deepcore to probe Earth's interior with atmospheric neutrino oscillations. Eur. Phys. J. Spec. Top. 234 (16), 5055–5064.

Chizhov, M., Maris, M., Petcov, S.T., 1998. On the oscillation length resonance in the transitions of solar and atmospheric neutrinos crossing the Earth core. arXiv:hep-ph/9810501

Coelho, J. A.B., Pestes, R., Domi, A., Bourret, S., Rahaman, U., Maderer, L., Carretero, V., 2023. joaoabcoelho/oscprob: v2.0.12. https://doi.org/10.5281/zenodo.10104847

Debayle, E., Dubuffet, F., Durand, S., 2016. An automatically updated s-wave model of the upper mantle and the depth extent of azimuthal anisotropy. Geophys. Res. Lett. 43 (2), 674–682.

Deng, X., Xu, Y., Hao, S., Ruan, Y., Zhao, Y., Wang, W., Ni, S., Wu, Z., 2023. Compositional and thermal state of the lower mantle from joint 3D inversion with seismic tomography and mineral elasticity. Proc. Natl. Acad. Sci. 120 (26), e2220178120.

Denton, P.B., Pestes, R., 2021. Neutrino oscillations through the Earth's core. Phys. Rev. D 104 (11), 113007. 2110.01148. https://doi.org/10.1103/PhysRevD.104.113007

Deschamps, F., Konishi, K., Fuji, N., Cobden, L., 2019. Radial thermo-chemical structure beneath western and northern Pacific from seismic waveform inversion. Earth Planet. Sci. Lett. 520, 153–163.

D'Olivo Saez, J.C., Lara, J. A.H., Romero, I., Sampayo, O.A., 2022. Oscillation tomografy study of Earth's composition and density with atmospheric neutrinos. Eur. Phys. J. C 82 (7), 614. 2207.11257. https://doi.org/10.1140/epjc/s10052-022-10563-y

Durand, S., Debayle, É., Ricard, Y., Lambotte, S., 2016. Seismic evidence for a change in the large scale tomographic pattern accross the d layer. Geophys. J. Int. 43 (15), 7928–7936.

Durand, S., Debayle, E., Ricard, Y., Zaroli, C., Lambotte, S., 2017. Confirmation of a change in the global shear velocity pattern at around 1000 km depth. Geophys. J. Int. 211 (3), 1628–1639.

Durand, S., Gaffet, S., Virieux, J., 1999. Seismic diffracted waves from topography using 3-D discrete wavenumber-boundary integral equation simulation. Geophysics 64. https://doi.org/10.1190/1.1444564

Dziewonski, A.M., Anderson, D.L., 1981. Preliminary reference Earth model. Phys. Earth Planet. Inter. 25 (4), 297–356.

Esteban, I., Gonzalez-Garcia, M.C., Maltoni, M., Martinez-Soler, I., Pinheiro, J.P., Schwetz, T., 2025. Nufit-6.0: updated global analysis of three-flavor neutrino oscillations. J. High Energy Phys. 2024 (12), 1–33.

Fichtner, A., 2010. Full Seismic form Modelling and Inversion. Springer Science & Business Media.

Fichtner, A., Kennett, B. L.N., Tsai, V.C., Thurber, C.H., Rodgers, A.J., Tape, C., Rawlinson, N., Borcherdt, R.D., Lebedev, S., Priestley, K., et al., 2024. Seismic tomography 2024. Bull. Seismol. Soc. Am. 114 (3), 1185–1213.

Formaggio, J.A., Zeller, G.P., 2012. From eV to EeV: neutrino cross sections across energy scales. Rev. Mod. Phys. 84 (3), 1307–1341.

French, S.W., Romanowicz, B., 2015. Broad plumes rooted at the base of the Earth's mantle beneath major hotspots. Nature 525 (7567), 95–99.

Fuji, N., Kawai, K., Geller, R.J., 2010. A methodology for inversion of broadband seismic waveforms for elastic and anelastic structure and its application to the mantle transition zone beneath the northwestern Pacific. Phys. Earth Planet. Inter. 180 (3–4), 118–137.

Giunti, C., Kim, C.W., 2007. Fundamentals of Neutrino Physics and Astrophysics. Oxford university press.

http://www-rccn.icrr.u-tokyo.ac.jp/mhonda/public/

Honda, M., Athar, M.S., Kajita, T., Kasahara, K., Midorikawa, S., 2015. Atmospheric neutrino flux calculation using the NRLMSISE-00 atmospheric model. Phys. Rev. D 92 (2), 023004.

Hosseini, K., Sigloch, K., Tsekhmistrenko, M., Zaheri, A., Nissen-Meyer, T., Igel, H., 2020. Global mantle structure from multifrequency tomography using P, PP and P-diffracted waves. Geophys. J. Int. 220 (1), 96–141.

Irving, J. C.E., Cottaar, S., Lekić, V., 2018. Seismically determined elastic parameters for Earth's outer core. Sci. Adv. 4 (6), eaar2538. https://doi.org/10.1126/sciadv.aar2538

Ishii, M., Tromp, J., 1999. Normal-mode and free-air gravity constraints on lateral variations in velocity and density of Earth's mantle. Science 285 (5431), 1231–1236. https://doi.org/10.1126/science.285.5431.1231

Jacob, A., Plasman, M., Perrin, C., Fuji, N., Lognonné, P., Xu, Z., Drilleau, M., Brinkman, N., Stähler, S., Sainton, G., Lucas, A., Giardini, D., Kawamura, T., Clinton, J., Banerdt, W.B., 2022. Seismic sources of insight marsquakes and seismotectonic context of elysium planitia, Mars. Tectonophysics 837, 229434. https://doi.org/10.1016/j.tecto.2022.229434

Jesús-Valls, C., Petcov, S.T., Xia, J., 2025. Neutrino oscillation tomography of the Earth with the Hyper-Kamiokande detector. Eur. Phys. J. C 85 (6), 703. 2411.12344. https://doi.org/10.1140/epjc/s10052-025-14338-z

Kelly, K.J., Machado, P. A.N., Martinez-Soler, I., Perez-Gonzalez, Y.F., 2022. Dune atmospheric neutrinos: Earth tomography. J. High Energy Phys. 2022 (5), 1–46.

Koelemeijer, P., Ritsema, J., Deuss, A., van Heijst, H.J., 2015. Sp12rts: a degree-12 model of shear- and compressional-wave velocity for Earth's mantle. Geophys. J. Int. 204 (2), 1024–1039.

Konishi, K., Fuji, N., Deschamps, F., 2020. Three-dimensional elastic and anelastic structure of the lowermost mantle beneath the western Pacific from finite-frequency tomography. J. Geophys. Res.: Solid Earth 125 (2), e2019JB018089.

Kopp, J., 2008. Efficient numerical diagonalization of hermitian 3×3 matrices. Int. J. Mod. Phys. C 19 (03), 523–548.

Kozlovsky, Y.A., Adrianov, N.I., 1987. The Superdeep Well of the Kola Peninsula. Springer.

Kuo, C., Romanowicz, B., 2002. On the resolution of density anomalies in the Earth's mantle using spectral fitting of normal-mode data. Geophys. J. Int. 150 (1), 162–179. https://doi.org/10.1046/j.1365-246X.2002.01698.x

http://www.lngs.infn.it/en.

Lognonné, P., Banerdt, W.B., Pike, W.T., Giardini, D., Christensen, U., Garcia, R.F., Kawamura, T., Kedar, S., Knapmeyer-Endrun, B., Margerin, L., Nimmo, F., Panning, M., Tauzin, B., Scholz, J.-R., Antonangeli, D., Barkaoui, S., Beucler, E., Bissig, F., Brinkman, N., Calvet, M., Ceylan, S., Charalambous, C., Davis, P., van Driel, M., Drilleau, M., Fayon, L., Joshi, R., Kenda, B., Khan, A., Knapmeyer, M., Lekic, V., McClean, J., Mimoun, D., Murdoch, N., Pan, L., Perrin, C., Pinot, B., Pou, L., Menina, S., Rodriguez, S., Schmelzbach, C., Schmerr, N., Sollberger, D., Spiga, A., Stähler, S., Stott, A., Stutzmann, E., Tharimena, S., Widmer-Schnidrig, R., Andersson, F., Ansan, V., Beghein, C., Böse, M., Bozdag, E., Clinton, J., Daubar, I., Delage, P., Fuji, N., Golombek, M., Grott, M., Horleston, A., Hurst, K., Irving, J., Jacob, A., Knollenberg, J., Krasner, S., Krause, C., Lorenz, R., Michaut, C., Myhill, R., Nissen-Meyer, T., ten Pierick, J., Plesa, A.-C., Quantin-Nataf, C., Robertsson, J., Rochas, L., Schimmel, M., Smrekar, S., Spohn, T., Teanby, N., Tromp, J., Vallade, J., Verdier, N., Vrettos, C., Weber, R., Banfield, D., Barrett, E., Bierwirth, M., Calcutt, S., Compaire, N., Johnson, C.L., Mance, D., Euchner, F., Kerjean, L., Mainsant, G., Mocquet, A., Rodriguez Manfredi, J.A., Pont, G., Laudet, P., Nebut, T., de Raucourt, S., Robert, O., Russell, C.T., Sylvestre-Baron, A., Tillier, S., Warren, T., Wieczorek, M., Yana, C., Zweifel, P., 2020. Constraints on the shallow elastic and anelastic structure of Mars from insight seismic data. Nat. Geosci. 13 (3), 213–220. https://doi.org/10.1038/s41561-020-0536-y

Maderer, L., Kaminski, E., Coelho, J. A.B., Bourret, S., Van Elewyck, V., 2023a. Earthprobe. https://gitlab.in2p3.fr/apc-tomography/earthprobe. Companion repository to "Unveiling the outer core composition with neutrino oscillation tomography".

Maderer, L., Kaminski, E., Coelho, J. A.B., Bourret, S., Van Elewyck, V., 2023b. Unveiling the outer core composition with neutrino oscillation tomography. Front. Earth Sci. 11, 1008396.

McDonough, W., 2010. Compositional model for the Earth's core. Read. Treatise Geochem.: Deriv. Treatise Geochem. .

Montagner, J.-P., Tanimoto, T., 1990. Global anisotropy in the upper mantle inferred from the regionalization of phase velocities. J. Geophys. Res.: Solid Earth 95 (B4), 4797–4819.

Olive, K.A., et al., 2014. Review of particle physics. Chin. Phys. C 38, 090001. And 2015 update available at https://doi.org/10.1088/1674-1137/38/9/090001

Petcov, S.T., 2024. Neutrino tomography of the Earth: the Earth total mass, moment of inertia and hydrostatic equilibrium constraints. Eur. Phys. J. C 84 (9), 991.

Quinby-Hunt, M.S., Turehian, K.K., 1983. Distribution of elements in sea water. Eos Trans. Am. Geophys. Union 64 (14), 130.

Ritsema, J., Deuss, A., van Heijst, H.J., Woodhouse, J.H., 2011. S40RTS: a degree-40 shear-velocity model for the mantle from new Rayleigh wave dispersion, teleseismic traveltime and normal-mode splitting function measurements. Geophys. J. Int. 184 (3), 1223–1236.

Romanowicz, B., 2001. Can we resolve 3D density heterogeneity in the lower mantle? Geophys. Res. Lett. 28 (6), 1107–1110.

Rott, C., Taketa, A., Bose, D., 2015. Spectrometry of the Earth using neutrino oscillations. Sci. Rep. 5 (1), 15225.

Sengupta, M.K., Toksöz, M.N., 1976. Three dimensional model of seismic velocity variation in the Earth's mantle. Geophys. Res. Lett. 3 (2), 84–86.

Tanabashi, M., Hagiwara, K., Hikasa, K., Nakamura, K., Sumino, Y., Takahashi, F., Tanaka, J., Agashe, K., Aielli, G., Amsler, C., et al., 2018. Review of particle physics: particle data groups. Phys. Rev. D 98 (3), 1–1898.

Tuli, J.K., et al., 1995. Nuclear Wallet Cards. Brookhaven National Laboratory Upton, NY.

Upadhyay, A.K., Kumar, A., Agarwalla, S.K., Dighe, A., 2023. Locating the core-mantle boundary using oscillations of atmospheric neutrinos. JHEP 04, 068. 2211.08688. https://doi.org/10.1007/JHEP04(2023)068

Virieux, J., Operto, S., 2009. An overview of full-waveform inversion in exploration geophysics. Geophysics 74 (6), WCC1–WCC26. https://doi.org/10.1190/1.3238367

Virieux, J., Operto, S., 2010. An overview of full-waveform inversion in exploration geophysics .

Wedepohl, K.H., 1995. The composition of the continental crust. Geochim. Cosmochim. Acta 59 (7), 1217–1232.

Winter, W., 2006. Neutrino tomography: learning about the Earth's interior using the propagation of neutrinos. Earth Moon Planets 99, 285.

Winter, W., 2016. Atmospheric neutrino oscillations for Earth tomography. Nucl. Phys. B 908, 250–267.